ABSTRACT

VUTHA, ASHWIN KUMAR. A Microfluidic Device for Thermal Flow Cytometry. (Under the direction of Dr. Glenn Walker and Dr. Clement Kleinstreuer).

Extensive efforts have been made in the development of devices applied to flow cytometry (Bonetta 2005, Graves et. al 2001, Chapman 2000). Several of these projects have been successful in miniaturizing such devices, while also saving time and expenses incurred in processes associated with cytometry (McPherson and Walker 2010, Lee et al. 2009, Zheng et. al 2008, Rodriguez-Trujillo et al. 2007). The resistive pulse method, impedance spectroscopy and light-based counters are commonly used to quantify particles in a fluid. In this thesis, a novel method is described for particle quantification, which makes use of thermal properties of solids in a liquid. In this method, a microfluidic device was fabricated, consisting of a silicon substrate and a polydimethylsiloxane (PDMS) mold that contained a microchannel. Nickel was deposited on the substrate, to form a resistance temperature detector. The two-wire resistance method was used to measure the change in resistance of the sensor due to difference in thermal properties of the constituents of the mixture used. Computational modeling of the system was performed, using COMSOL Multiphysics software.

A Microfluidic Device for Thermal Flow Cytometry

by
Ashwin Kumar Vutha

A thesis submitted to the Graduate Faculty of
North Carolina State University
in partial fulfillment of the
requirements for the degree of
Master of Science

Mechanical Engineering

Raleigh, North Carolina

2013

APPROVED BY:

_____	_____
Dr. Clement Kleinstreuer	Dr. Glenn Walker
Committee Co-Chair	Committee Co-Chair

_____

Dr. Amassa Fauntleroy

BIOGRAPHY

The author was born in the city of Mumbai, on the western coast of India. After obtaining his Bachelor's degree in Mechanical Engineering at the University of Mumbai, he worked in the manufacturing sector in India for a little under a year, before moving to the U.S to pursue a Master's degree. Having had an enriching experience while engaged in research, he intends to pursue a doctoral degree in Mechanical Engineering, beginning Fall 2013.

ACKNOWLEDGMENTS

I would like to extend my heartfelt gratitude to Dr. Glenn Walker and Dr. Clement Kleinstreuer for giving me the opportunity to take up this exciting and challenging project as well as for lending their expertise and precious time for feedback and suggestions. I would also like to thank the following people for their valuable contribution(s) towards the completion of this thesis - Dr. Amassa Fauntleroy for agreeing to be part of my committee; Dr. Chung Hoon Lee and his research group for some fantastically fabricated substrates; Dr. Paul Ro, for awarding me a teaching assistantship; Vindhya Kunduru, Amy McPherson and Prithwish Kundu, for the invaluable tips and suggestions; Annie White, Crystal Blackford and Marilyn Cross in the department graduate office for handling the paperwork smoothly, which kept me on schedule from the beginning to the end.

TABLE OF CONTENTS

LIST OF TABLES

LIST OF FIGURES

Chapter 1

Introduction

1.1 History of Flow Cytometry

Flow cytometry can be defined as the process of evaluating the physical and/or chemical properties of biological cells, when they are suspended in a dynamic fluid. The invention and use of flow cytometers dates back several decades. The concept of particle or cell counting has roots much further back in history. Since the 1600s, microscopes have been used to study cells, tissues and other biological matter. With the development of stains in the late nineteenth century, fluorescence microscopy began gaining attention for several specific applications. In the 1940s, the work of Albert Coons in labeling antibodies with fluorescent tags provided impetus for the growth in use of fluorescence for various applications. Fluorescence microscopy is now one of the most commonly used techniques for particle analysis in the biological sciences. A source of light is attached to microscopes along with a filter, to stimulate the fluorescent chemical and facilitate observation (Givan 2001).

Andrew Moldovan was one of the first to suggest the use of dynamic fluid-particle suspensions for biological analysis (Shapiro 2003). His proposed apparatus was intended to be used to screen red blood cells or yeast cells as they passed through a thin capillary, under a microscope. The microscope was to be fitted with a photodetector, which would record the presence of a cell on the basis of light obscuration.

While it is uncertain whether Moldovan actually built a device for this purpose, it came to be known that the technique he suggested could be suitably adopted for such analysis. Moldovan's proposal laid the foundation for much of the later instrumentation for flow cytometry. In 1965, Kamentsky and Melamed tried to improve on Moldovan's idea through the use of a spectrophotometer that recorded the ultraviolet (UV) absorption and scattering of blue light by cells flowing past a microscope objective at speeds exceeding 500 cells/s. This was followed by Dittrich and Göhde in 1969, who developed a flow chamber that could generate histograms of fluorescence intensity, based on the fluorescence of the DNA of alcohol-fixed cells (Givan 2001).

In 1949, Wallace Coulter filed for a patent on a device he developed, that was capable of detecting microscopic particles in a carrier fluid, specifically, blood. The patent was approved in 1953 and since then, it has been one of the most significant inventions in the field of flow cytometry. It forms the basis for present day pathological tests which involve a blood count.

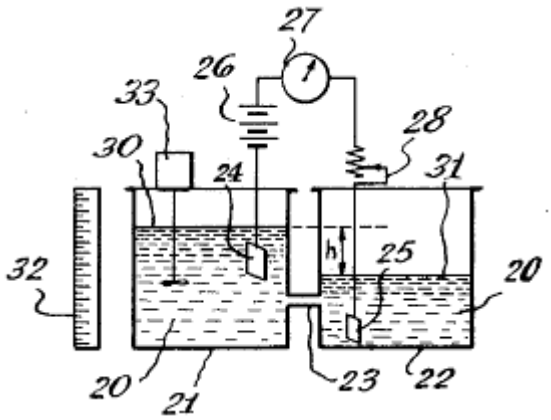

Figure 1.1: The Coulter Counter, developed by Wallace Coulter in the 1940s. The device was designed to allow the flow of a particulate suspension through a narrow orifice under a pressure head. A voltage potential is applied across the orifice. As particles flow through, the electrical impedance across the orifice increases and results in a drop in measured current. The diameter of the orifice depends on the diameter of the particles to be counted. The description of the components indicated by the numbers can be found in (Coulter 1953, U.S Patent 2,656,508).

The working of the Coulter Counter can be explained as follows - an electrolytic fluid containing suspended particles is made to flow through a channel of small length and with a small bore, as shown in Fig 1.1. This may be done by means of two vessels, with a pressure difference between them. The fluid flows from the vessel at higher pressure to the one at lower pressure through the orifice. Two electrodes are used, one in each vessel and the free ends of the electrodes are electrically connected via the bore. The fluid flowing through the channel completes the electrical circuit. A constant current is made to flow through the circuit.

Assuming that the electrical conductivities of the fluid and the dissolved particles are different, the presence of a particle in the channel will form a temporary partial or complete obstruction to the flow of current and this will cause a sharp change in current for the duration that the particle is in the channel. This method can be applied to a suspension containing particles of different types as well as one containing suspended particles of the same type. One of the important considerations in the use of such a device is that the particles to be counted must remain suspended in the carrier fluid without settling. Additionally, the length of the conduit or channel must be as short as possible to avoid the presence of multiple particles in the channel at the same instant (or minimize coincidence). This concern is also to be addressed by means of the concentration of the mixture. Dilute solutions are better suited for evaluation than concentrated ones. Fig 1.2 shows the effect of presence of a particle on the signal recorded by a Coulter Counter.

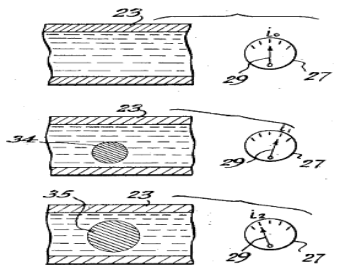

Figure 1.2: Cross-sectional view of the channel without and with the presence of a particle (Coulter 1953, U.S Patent 2,656,508). With no particle, the gauge shows the constant value of the current supplied. For particles of different sizes, the gauge experiences different deflections.

1.2 Miniaturization of the Coulter Counter

Although the original Coulter Counter was and continues to be a reliable resource for particle counting, researchers in the recent past have realized that its benefits could be increased by miniaturizing it. A 'micro Coulter Counter', in addition to the existing features of the full-scale counter, would be portable, much less expensive and quicker in producing results. It would also consume considerably smaller amounts of the analyte and buffer. Advancements in the field of micro-electromechanical systems (MEMS) have greatly facilitated efforts to produce such miniature particle counters. MEMS-based Coulter Counters can be produced in batches and are easy to fabricate. It is also convenient to add more functionalities to existing designs. The materials involved are often inexpensive and easily available. Small-scale counters also enable parallelization, that is, connecting several microchannels in parallel for simultaneous analysis of multiple samples. Since they are inexpensive, these counters can be disposed after using them once for a counting task which reduces cross-contamination of samples.

With the goal of improving on the original Coulter Counter as described above, several researchers have made attempts at fabricating microscale Coulter Counters for particle detection. Fig 1.3 shows the first 'Microchip Coulter Particle Counter (μCPC)' which was based on the Coulter's principle, produced by Larsen, Blankenstein and Branebjerg (Larsen et. al 1997).

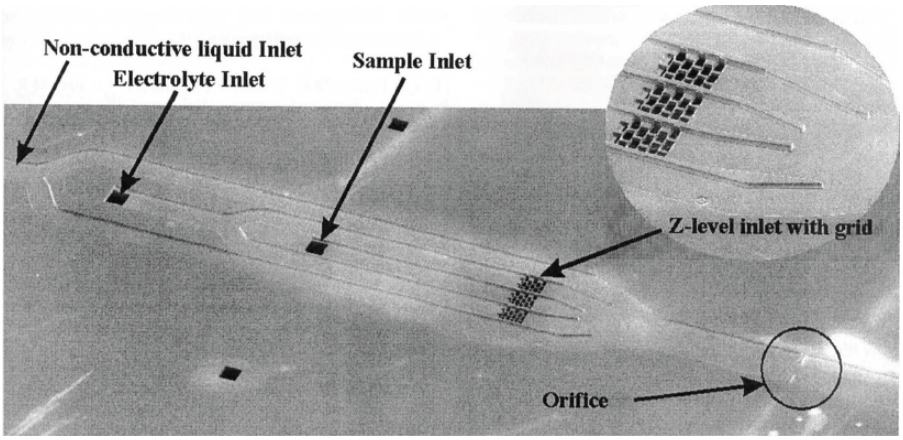

Figure 1.3: The first microfluidic Coulter Counter developed (Larsen et. al 1997). Channels were fabricated by etching on a silicon substrate. Hydrodynamic focusing was applied by using a sheath fluid on either side of the sample. The electrodes were damaged during operation and therefore no repeatable results were possible.

In Larsen's design, microchannels for fluid flow were etched into a silicon substrate using RIE in SF_6/O_2 plasma. The electrodes used were made of gold and were bonded to a glass wafer using electrostatic sealing. The device made use of hydrodynamic focusing in which the electrolyte or sample was sheathed by a non-conductive fluid on either side. The sample, which was an electrolyte containing cells, was injected into the inlet and was focused into one stream of cells, using the sheath fluid. The use of such focusing was found to significantly reduce clogging in the channels. Initial tests showed that accurate control of the sheathing process is possible and it was found that this could be used to increase the sensitivity range of Coulter's principle.

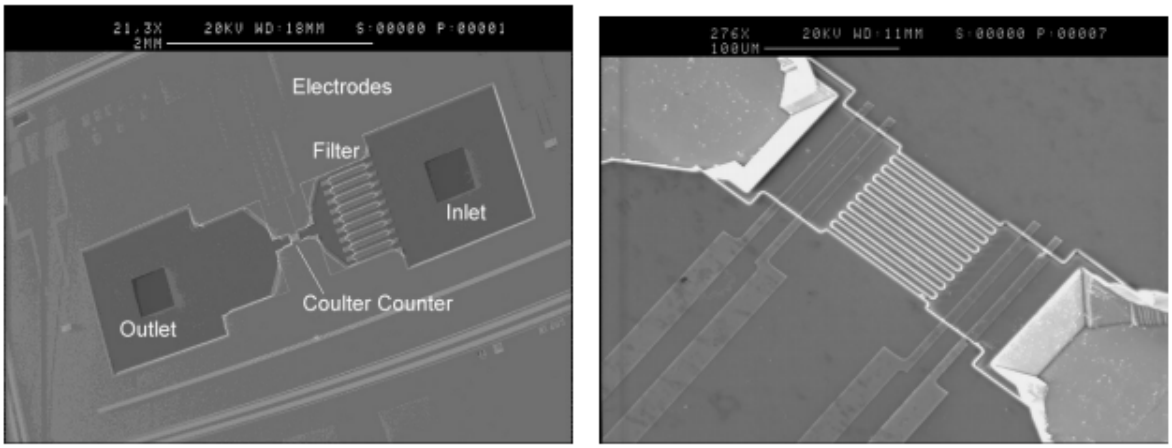

(a) (b)

Figure 1.4: (a) Layout of the device developed by Koch et. al (1999). The inlet is to the right, the outlet to the left and the electrodes on top. The electrodes are not clearly visible because they are embedded between layers of silicon nitride. Fig 1.4 (b) shows a magnified view of the device with two electrodes are each end of the channel structure, to facilitate four-point measurements.

Following the pioneering work done by Larsen et. al in miniaturizing the Coulter Counter, a micromachined Coulter Counter (Fig 1.4) was developed by Koch et. al (1999). The device was similar to its predecessor in that it had channels etched into a silicon substrate but in contrast, Ti/Au electrodes were used instead of gold electrodes. The device was designed in a manner that would allow the integration of a micromixer onto the same chip.

The original Coulter Counter operated using the resistive pulse sensing (RPS) technique. As described earlier, in this method, the passage of a particle past a detection region that is

supplied a constant current, produces a sharp pulse or change in the electrical resistance of the circuit which is connected to the detection region. The number of pulses indicates the number of particles that have crossed the detection region. Over a period of several years, this technique has been widely employed at the microscale (Larsen et. al 1997), (Koch et. al 1999), (Carbonaro and Sohn 2005), (Jagtiani et al. 2006), (Xu et al. 2007). It has also been further miniaturized for use at the nanoscale (Zhang et al. 2009), which allows counting of DNA/RNA.

1.3 Methods for Particle Counting in Microchannels

Capacitance Counters

While the Coulter principle may be successfully applied toward detection of particles in common carrier fluids like water or other biological fluids, it is difficult to use when the base medium has low electrical conductivity, as in the case of oil (Murali et al. 2009). The solution proposed by Murali et. al to this limitation was to measure the change in capacitance between two electrodes placed in the channel, when a particle passed through it. Fig 1.5 shows a top view and sectional front view of their capacitance counter. The electrodes were separated by a distance of 20 μm. Aluminum particles between 10 μm and 25 μm were used in the test. This method was used to monitor the presence of metal particles resulting from wear, in lubrication oil. The change in capacitance occurs due to the difference in permittivity of the lubricating oil and the particles.

The capacitance counter has similar advantages to the resistive pulse counter in terms of ease of use, low cost, small dimensions and reliability. In addition, it can also be used to analyze the polarization response of both organic as well as inorganic substances in an electric field.

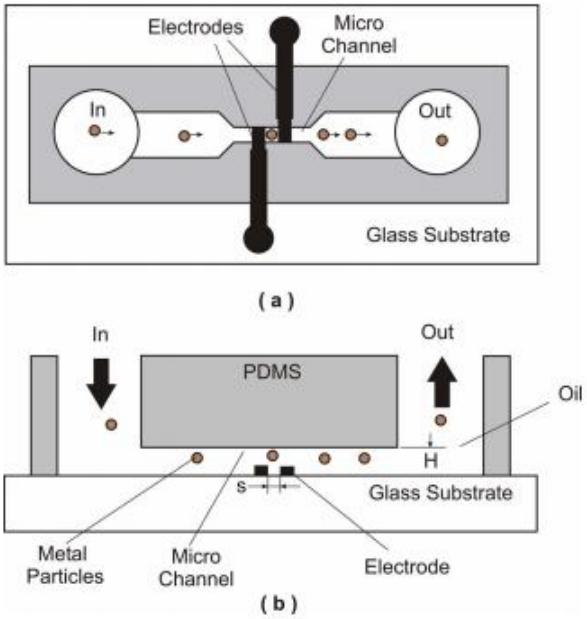

Figure 1.5: The microfluidic counter developed by (Murali et al. 2009). (a) Top view and (b) Sectional front view.

Impedance Spectroscopy

Impedance spectroscopy relies on the measurement of change in impedance of a circuit due to the passage of particle (Gawad et. al 2001). As shown in Fig 1.6, the passage of a cell causes a change in impedance Z_{AC} while Z_{BC} remains unaffected.

The signal Z_{AC} - Z_{BC} is measured as the cell passes consecutively between each pair of electrodes. One feature of this method is that it allows calculation of the speed of the particle by measuring the distance between the electrodes and the time between the peaks seen in the signal. Using this information, the height of the particle in the channel can be determined through the flow profile of the fluid.

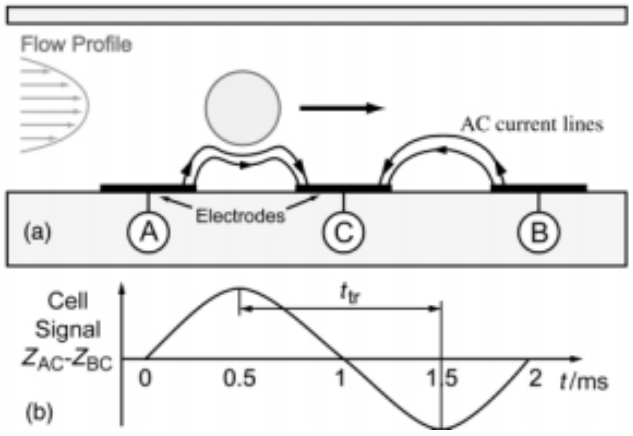

Figure 1.6: (a) Schematic of impedance spectroscopy used to count and characterize cells (Gawad et. al 2001). The impedance measurement is made differentially between two pairs of electrodes, AC and BC. (b) The impedance signal obtained from (a) allows calculation of the speed of the particle.

Light-scattering and light-blocking particle counters

The interaction of particles in a fluid, with light, can also be used for their quantification and analysis. Two such counters are the light-blocking and light-scattering counters (Zhang et al. 2009).

Rays of light striking a particle experience a combination of transmission, reflection and absorption. The proportion of each component in the process depends on the optical properties of the particles involved. A schematic of both types of particle counters is shown in Fig 1.7. In the case of light-scattering counters, photodetectors are placed at small angles to the path of light from the source to the particle. When the light strikes the particle, a part of it gets reflected onto the detector and a pulse is registered. The number of pulses determines the number of particles that have passed by the detector. The intensity of the pulse scales with the size of the particle. In light-blocking counters, the light is focused directly onto the detector. When a particle passes through the region between the source and the photodetector, the region behind the particle experiences lesser intensity of light. The number of low-intensity spots can be used to determine the number particles. The larger the particle, the lower the intensity of light in the blocked region. The light-scattering counter is more sensitive than the light-blocking counter but it is more expensive and more complex. The working of both the light-based counters depends on the surface area of the particles involved, which makes them less sensitive than those counters employing the RPS technique, since they utilize the volume of the particles. Pamme et. al (2003) used the light-scattering technique for detection of biological matter while Xiang et. al (2005) used the light-blocking counter for detection of microparticles in a microchannel.

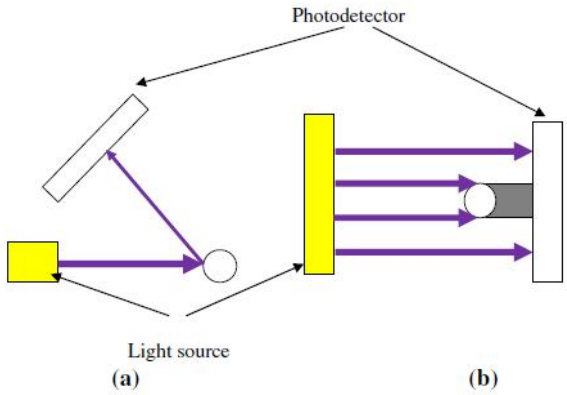

Figure 1.7: Schematic for (a) Light-scattering particle counter and (b) Light-blocking particle counter (Zhang et al. 2009).

Counters based on Fluorescence

The use of fluorescence to identify and characterize particles in a fluid medium has been a relatively recent practice. Fluorescence is the phenomena in which a substance absorbs light of some wavelength and emits light of a different wavelength. In special cases, the wavelength of the emitted light may be the same as that of the light absorbed and this is referred to as 'resonance fluorescence'. When a fluorescent particle absorbs light, it transitions to a higher energy level and when it returns to its original state, it emits light whose energy is proportional to the difference in energy levels of the ground-state and excited state of the particle. Fig 1.8 shows the schematic of a fluorescence-based microfludic flow cytometer developed by Lin and Lee (2003). A number of cells or particles are suspended in a fluid stream and made to flow single-file through a channel.

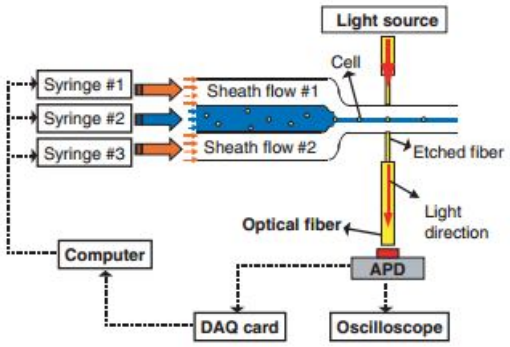

Figure 1.8: Schematic of the microfluidic flow cytometer based on fluorescence. Cells are hydrodynamically focused through the detection region. Light from the source is scattered by the cells and the APD converts the optical signals to electrical signals (Lin & Lee 2003).

The particles are hydrodynamically focused into the detection region. A beam of light, usually laser, is focused either perpendicular to the stream in such a way that the particles enter the region of the beam one at a time. A light detector such as a photomultiplier tube is placed close to the region of the beam so that it detects the emission of light from each particle.

One of the earliest optical microflow cytometers was developed by Altendorf et al. (1996). They made use of microfabricated V-grooves in a silicon substrate along with a laser diode and photodiode detector for detection of the scattered light. Cui et. al (2002) made use of interdigitated electrodes to produce a non-uniform electric field that caused particles to move under the influence of either Dielectrophoresis (DEP) or Travelling Wave Dielectrophoresis

(twDEP). Particles could be detected either by sensing scattered light or fluorescence emission from a particle labeled with appropriate material. The working principle of the device is shown in Fig 1.9. A particle crossing the light source absorbs light at the excitation wavelength and emits light of a longer wavelength which is detected by a photodiode. Fig 1.10 displays the signal obtained through the fluorescence emission from a 15 μm particle. Optical fibers were fixed 2 mm apart in grooves perpendicular to the direction of flow.

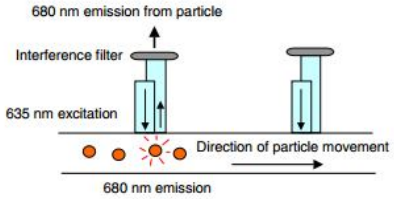

Figure 1.9: Schematic of the fluorescence-based device developed by (Cui et. al 2002). The light emitted from the particle has a longer wavelength than the incident light.

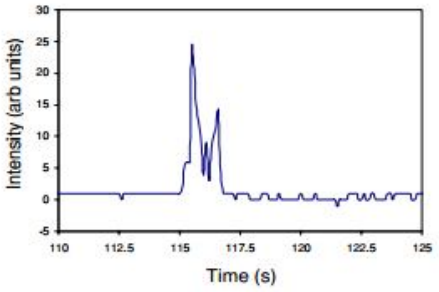

Figure 1.10: The intensity of light emitted from a 15 μm particle as detected by a light detector. (Cui et. al 2002).

1.4 Research Objectives and Novel Contributions

The background provided above serves as an overview of the commonly used techniques to count and/or characterize sub-micron particles in suspensions. Several other techniques exist and new techniques continue to be developed as the field of diagnostics expands. The existing methods of particle counting have various limitations and are most appropriate for specific applications. For example, techniques such as light scattering/blocking, flow microscopy etc. which make use of differences in optical parameters (such as refractive index) between particle and suspension may be inaccurate for applications involving solid particles which are translucent. This may be seen during quantification of sub-visible protein particles, particularly in concentrated solutions where the refractive index of the solution may nearly equal that of the protein (Patel et. al 2012). Tried and tested methods like the Coulter Counter with the resistive pulse sensor are difficult to scale up for parallel quantification because this involves connecting together the circuits for individual channels and this leads to electrical 'cross-talk' between channels. Additionally, the conventional Coulter Counter method is difficult to use when the base fluid has low electrical conductivity, such as machine oil (Murali et al. 2009). Capacitance-based counters, which are used as alternatives to the Coulter counter, have limitations, such as charge-screening effect at the interface of the electrode and the carrier fluid, which may distort the readings obtained. Also, auxiliary equipment such as a frequency modulation controller is required (Zhang et al. 2009). Optical spectroscopy can be used to count and characterize cells accurately in the sub-micron range

but it requires the use of optical 'tags' and is limited to a few different colors. Additionally the presence of such tags in the form of dyes or other chemicals on the particles means that they cannot be reused.

The objective of this thesis is to present a novel method called Thermal Flow Cytometry (TFC), which can overcome several or all of the limitations mentioned above. The method does not rely on electrical or optical properties of particles and carrier fluids and can therefore be applied in counting metallic particles in lubricant oils or biological matter in translucent solutions. It is also suitable for large scale parallel quantification since cross-talk in this case can be avoided through suitable design of heaters/sensors. It is inexpensive, easy to setup and use, offers quick response time and results can be obtained within minutes.

The idea of using the thermal response of a substance for its characterization has been successfully implemented by Choi and Kim (2008) and Namwoo et. al (2011). The technique employed by Choi and Kim was used to determine the thermal conductivity and heat capacity of fluid samples on the order of nanoliters. Namwoo et. al used a similar technique to quantify and characterize micro-droplets containing a mixture of bovine serum albumin (BSA) and deionized (DI) water. The fluid samples occupied the entire volume of the channel while the micro-droplets occupied most of the width and height. They were therefore large compared to the sensor, making them easier to detect as compared to solid particles used in flow cytometry.

TFC is proposed to quantify solid particles in a liquid medium, where the particle size is much less than the dimensions of the channel.

The concept of TFC is illustrated in Fig 1.11 (a). Liquid containing suspended solid particles is made to flow through a microchannel which is heated from the bottom. The liquid and the solid are heated at different rates as they pass over the heater. This is due to the difference in thermal properties of the liquid and the solid. Consider two scenarios as presented in Fig 1.11 (b) and (c)- the first scenario is that of liquid flowing through the microchannel without any solid particles while the second is that of liquid flowing with solid particles suspended in it. If we analyze an instant in time after the channel has been fully wetted, in the first case, we have a fixed volume of liquid directly above the heater region. This volume of fluid has absorbed a certain quantity of heat from the heater, thereby cooling it. In the second case, we may consider that a fraction of the volume of fluid in the first case has been replaced by an equivalent volume of solid, which is made up of thermally insulating material. The total volume of the liquid-solid mixture above the heater now has reduced capacity to absorb heat from the heater due to the insulating nature of the solid. This causes a change in temperature of the heater for the duration that the solid is present above it. Once the solid has passed the heater, it is replaced by liquid and this brings down the temperature of the heater to a value until the next solid particle passes over it. The reverse is true in case of a solid which is a good thermal conductor, i.e, the temperature of the heater in the second case will be lower than that observed in the first case.

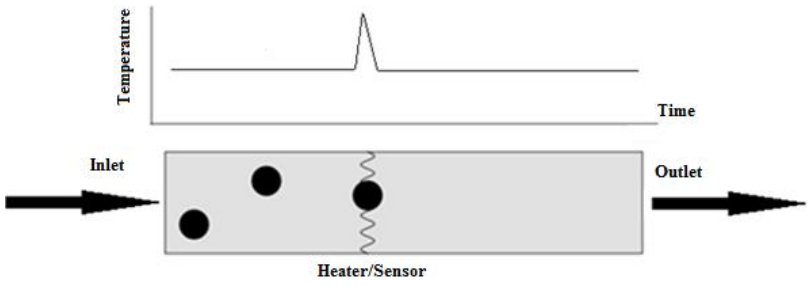

Figure 1.11: (a) Representative schematic of concept of TFC. The passage of a particle over the sensor produces a local change in temperature, which is registered by the sensor. The change can be viewed on a temperature-time plot at an arbitrarily selected point in the region just above the sensor.

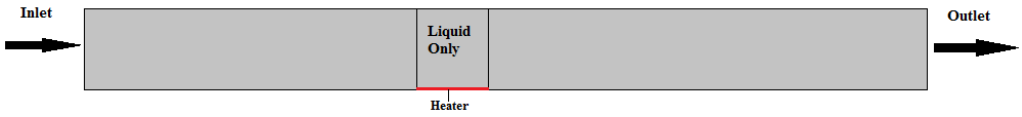

Figure 1.11: (b) TFC setup with only liquid flowing through the microchannel. At any instant in time after the channel has been wetted, there is a fixed volume of liquid in contact with the heater.

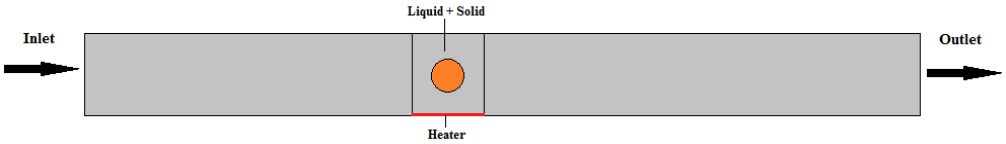

Figure 1.11: (c) TFC setup with liquid-solid mixture flowing through the microchannel. The volume of the mixture above the heater has different thermal properties compared to the volume of liquid only, in 1.9 (b).

Chapter 2

Computational Model

This chapter presents a computational approach to simulate the concept of TFC as described in section 1.4. The system sketch, assumptions and governing equations are described in section 2.1 while sections 2.2, 2.3 and 2.4 discuss the implementation of the model using COMSOL Multiphysics software.

2.1 Theory

TFC was by combining three domains in physics - laminar fluid flow, heat transfer and particle dynamics. Fig 2.1 shows the 2D representation of the system. The following assumptions/simplifications were made:

- A 2D model was deemed sufficient to understand the concept of TFC. This is because the relevant physics can be described in a 2D model, while reducing high computational time and cost associated with a 3D model.
- The boundary of the particle was treated as thermally insulating. This was a reasonable approximation since polystyrene has poor thermal properties (C_p~ 1.2 J/g-K, k ~ 0.14 W/m-K) and is treated as insulating material (Gaur, Wunderlich 1982, Marcus, Blaine 1994).

- No material properties were assigned to the particle, since the motion of the particle could be adequately simulated using a hollow circle. In addition, since the particle boundary was thermally insulating, no thermal properties were required to be specified for the particle.
- The effect of gravity on the particle was neglected.

In accordance with the above description and assumptions, the governing equations for the system were as follows:

2D continuity equation for an incompressible fluid:

$$\frac{\partial u}{\partial x} + \frac{\partial v}{\partial y} = 0 \tag{1}$$

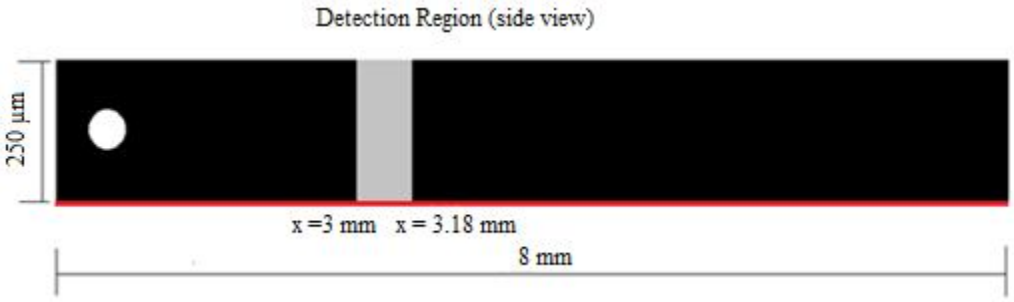

Figure 2.1: Geometry chosen for the computational model. The channel length and height were 8 mm and 250 µm respectively. The detection region (gray) was 180 µm long, between x=3 mm and x=3.18 mm. The particle (white) diameter was 90 µm. The red line at the bottom represents the heat flux applied as a rectangle function, which is described in section 2.2.

2D Navier-Stokes equation for laminar flow with constant fluid properties:

$$\rho \frac{\partial u}{\partial t} + u \frac{\partial u}{\partial x} + v \frac{\partial u}{\partial y} = -\frac{dp}{dx} + \upsilon \frac{\partial^2 u}{\partial y^2} \tag{2}$$

subject to

$$u(x, y, 0) = 0 \tag{3}$$

$$u(x, 0, t) = 0 \tag{4}$$

$$u(x, b, t) = 0 \tag{5}$$

$$v(x, 0, t) = 0 \tag{6}$$

$$v(x, b, t) = 0 \tag{7}$$

$$u(0, y, t) = f(t) \tag{8}$$

$$\mu(\nabla u + (\nabla u)^T)_{|(a, y, t)} = 0 \tag{9}$$

$$p = p_{0|(a,y,t)} \tag{10}$$

2D energy equation where temperature T = T (x,y)

$$\frac{\partial T}{\partial t} + u\frac{\partial T}{\partial x} = \alpha\left(\frac{\partial^2 T}{\partial x^2} + \frac{\partial^2 T}{\partial y^2}\right) \tag{11}$$

subject to

$$T\left(x, y, 0\right) = T_0 \tag{12}$$

$$T\left(0, y, t\right) = T_0 \tag{13}$$

$$k\Delta T_{|(a,y,t)} = 0 \tag{14}$$

$$\frac{\partial T}{\partial y}\left(x, b, t\right) = 0 \tag{15}$$

$$\frac{\partial T}{\partial y}\left(x, 0, t\right) = f\left(x,t\right) \tag{16}$$

where a= 8 mm, b =0.3 mm, T_0 = 293.15 K

The force acting on the particle is given by Newton's second law –

$$\sum \bar{F} = m_p \frac{d\bar{v}_p}{dt} \tag{17}$$

where is the mass and is the velocity of the particle. forces acting on the particle were calculated by integrating the fluid stresses over the boundary of the particle.

$$\sum \bar{F} = \int_{cs} \tau_w \, n \, ds - \int_{cs} p \, n \, ds \tag{18}$$

The boundary of the particle was treated as a moving wall whose x and y components of velocity were determined by eqs.(19) & (20).

$$F_x - m_p \frac{du_p}{dt} = 0 \tag{19}$$

$$F_y - m_p \frac{dv_p}{dt} = 0 \tag{20}$$

subject to the initial conditions $u_p(0) = 0$ and $v_p(0) = 0$.

2.2 Numerical Model

COMSOL Multiphysics software was used to solve the governing equations described in section 2.1. The model was setup using four modules - Laminar fluid flow, Global ODEs & DAEs, Moving Mesh, and Heat transfer in fluids. The laminar flow module was used to solve for the flow field. The Global ODEs and DAEs module was used to solve for particle motion based on Newton's second law. The Moving Mesh module made use of mesh movements to represent the displacement of the particle. The Heat transfer in fluids module solved for the temperature profile based on the flow field. All the above physics modules were solved simultaneously and were fully coupled. Results were obtained for three different inlet velocities of the fluid. In accordance with the parameters from the experiments, average inlet velocities of 1.33, 2 and 2.66 mm/s, corresponding to volumetric flow rates of 6, 9 and 12 µl/min respectively were used. The volumetric flow rates were converted to average velocities using the relation

$$Q = v.A \tag{21}$$

where Q is the flow rate in m^3/s, is the average velocity in m/s and A is the cross-sectional area of the channel in m^2.

The fluid used was water. For water, = 1000 kg/m^3, μ = 8.9 x 10^{-4} Pa-s at 25°C and the hydraulic diameter for the rectangular duct and Reynolds number for the flow were calculated using eq. (22) and (23) respectively.

$$d_h = \frac{2pq}{p+q} \tag{22}$$

$$Re = \frac{\rho\, u\, d_h}{\mu} \tag{23}$$

where 'p' and 'q' are the sides of the rectangular cross-sectional area of the channel. Here, p= 300 μm and q = 250 μm. The Reynolds numbers for the inlet velocities of 1.33, 2 and 2.66 mm/s, were found to be 0.448, 0.674 and 0.896 respectively. An average velocity boundary condition was specified for the fluid at the inlet of the channel. The fluid was initially held stationary for 5s while the heat flux was applied and ramped up to the specified value over 1s. The velocity was then ramped up in time to the specified value. At the outlet, the 'pressure, no viscous stresses' condition was specified, which is physically equivalent to the fluid being released into a large stationary reservoir. The boundary of the particle was treated as a moving wall, the x and y velocity components of which, were determined by the output of the Global ODEs and DAEs module. The same velocity components were specified in the moving mesh module to describe the mesh displacements.

The motion of the particle produced large deformation of the mesh, leading to potential problems with convergence. Hence, as shown in Fig 2.2, Bezier curves were used to 'assist' the moving mesh. These curves essentially prevent the formation of inverted mesh elements which may cause the solution to diverge. The speed of movement of the vertical lines was set equal to that of the particle. The horizontal lines were parametrically setup such that the line on the right of the particle reduced in length as the particle moved from left to right, while the line on the left increased in length. The solver was set to automatically remesh the domain when the specified condition of minimum mesh element quality was satisfied. Minimum element quality is essentially a measure of the symmetry of the mesh element, which goes from 0 to 1, with 1 with a perfectly symmetrical element and 0 being a degenerated element.

The minimum element quality was set to 0.2, which forced the solver to remesh the domain every time the element quality dropped below this value. At 2.66 mm/s, the solver was run for 7.2s with a time step of 0.01 for fluid velocity of 2.66 mm/s. At 1.33 mm/s and 2 mm/s, the solver was run for 7.5s and 7.4s respectively to allow the particle sufficient time to cross the heater.

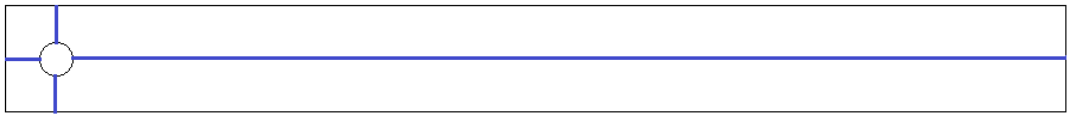

Figure 2.2: Bezier curves used to supplement the moving mesh. A in-built curve parameter 's' in COMSOL allows parametric conditions to be specified for the curves, which provide additional constraints that prevent inverted mesh elements.

The heater was modeled by means of a rectangle function (Fig 2.4) whose value was 1 in the region defined by the heater in the channel and was 0 everywhere else. The heat flux value was multiplied by this rectangle function so that the heat flux was non-zero only in the region of the heater. The heat flux was applied from t = 0 and allowed to ramp up to the maximum value over a time of 1s. A temperature boundary condition was set at the inlet, for the heat transfer module, and an outflow boundary condition was specified at the outlet, which assumes that convection dominates over diffusion across the outflow boundary.

The following parameters were used for the simulation and were selected to match the experimental parameters:

(a) mean radius of particle r_p= 90 μm

(b) average inlet velocities of fluid = 1.33, 2 and 2.66 mm/s

(c) length of the channel = 8 mm

(d) height of the channel = 250 μm

(e) Heat flux: The heat flux used in the computational model had to be approximated from the experimental setup. In the experiments, a current of 1 mA was passed through the RTD by the multimeter, which generated heat that was then dissipated upward into the microchannel as well as downward into the silicon nitride membrane and silicon substrate. To determine the magnitude of the heat flux in both directions, a 3D model was setup in COMSOL as shown in Fig 2.3. A steady analysis was performed by considering a test section from the experimental setup. The test section included the silicon nitride membrane, the RTD and the volume of water above the membrane. Based on the heat flux supplied the magnitudes of the heat flux at heights of 1 μm above and below the sensor were ~ 800 W/m^2 and 1.6 x 10^5 W/m^2 respectively.

(f) The RTD was treated as a heat source and a volumetric heat flux was supplied in W/m^3. The volumetric heat flux was calculated using the relation

$$Q_v = \frac{P}{V} \tag{24}$$

where P is the power dissipated by the RTD and is given by

$$P=i^2R \tag{25}$$

'i' is the current of 1 mA through the RTD and 'R' is the resistance of the RTD ~ 670 Ω

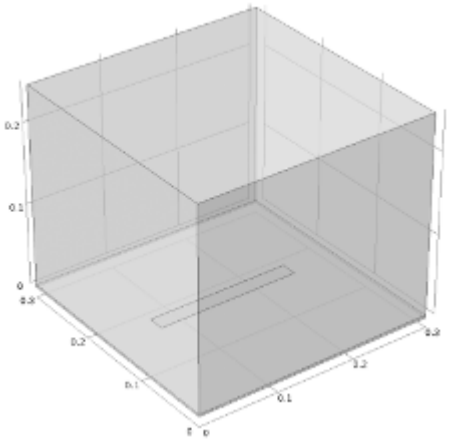

Figure 2.3: The 3D setup in COMSOL to determine the value of heat flux from the experiments. The square silicon nitride membrane of 300 μm side was at the bottom, the RTD above the membrane was 180 μm long, 20 μm wide and 200 nm high. The large block above the RTD is the volume of water that is in contact with the membrane at any given time.

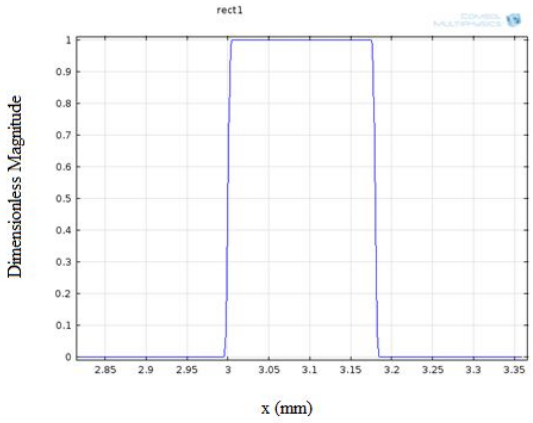

Figure 2.4: The heat flux specified in the form of a rectangle function that goes to 1 between x=3 mm and x= 3.18 mm and 0 elsewhere.

2.3 Computational Results

The velocity and temperature profiles were obtained for each of the inlet velocities stated in section 2.2. Figs 2.5 and 2.6 show representative velocity and temperature profiles for a 90 µm particle with fluid entering the inlet at an average velocity of 9 µl/min or 2 mm/s. To obtain a signal as the particle moves over the heater region, a point was probed 50 µm above the heater and the temperature was plotted against time at this point for each particle size and at each chosen inlet velocity. Fig. 2.7 displays a magnified image of the moving mesh at an arbitrarily selected time from the solution.

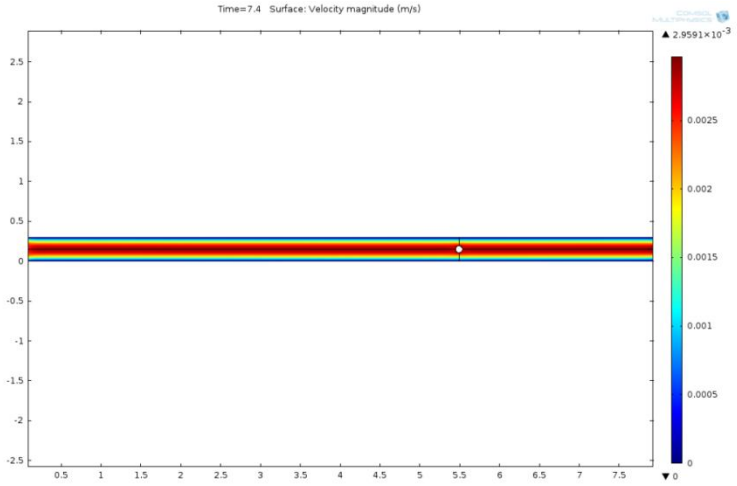

Figure 2.5: Velocity profile for 90 µm particle with average fluid inlet velocity at 2 mm/s.

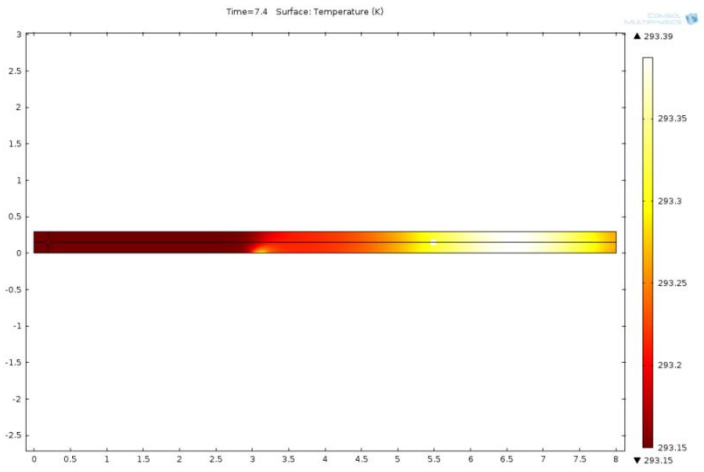

Figure 2.6: Temperature profile for 90 µm particle with average fluid inlet velocity at 2 mm/s.

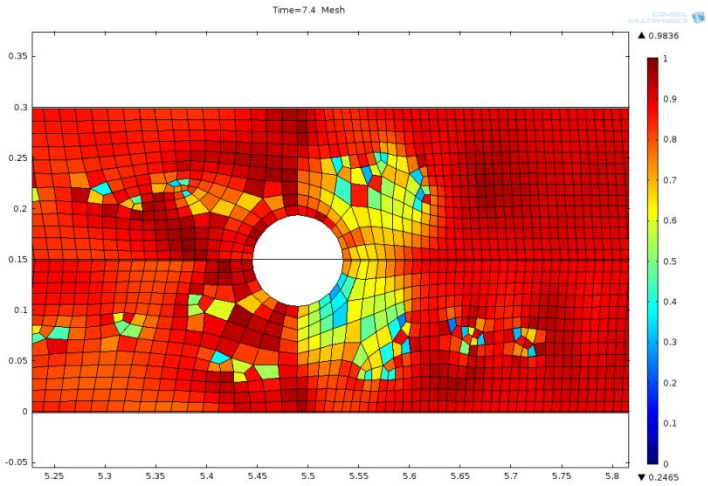

Figure 2.7: Magnified image showing mesh element deformation around the particle at t = 7.4s. The axis on the right indicates the extent of deformation, with 0 representing a completely degenerate element and 1, a perfectly symmetrical element.

The signals obtained for a 90 µm particle at fluid velocities of 1.33, 2 and 2.66 mm/s are shown in Figs. 2.8, 2.9 and 2.10 respectively. Since the fluid was held stationary for 5s while the heat flux was ramped up, the temperature rises initially and then begins to drop once the fluid starts to flow. The particle velocity increases with increase in velocity of the fluid, the time of residency of the particle over the heater/sensor reduces. Hence, the temperature peaks become narrower with increase in velocity of the particle or in other words, the fluctuation of temperature occurs over a shorter time interval.

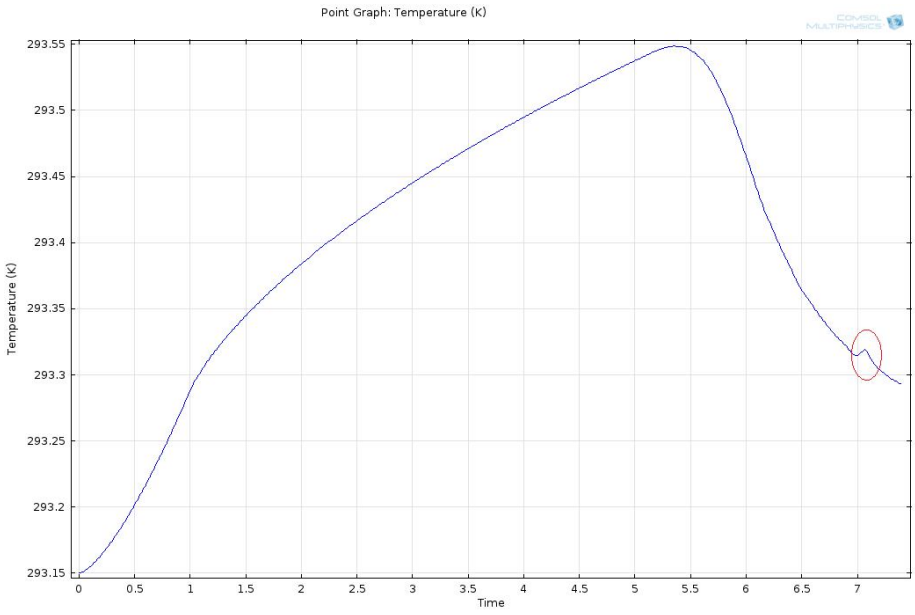

Figure 2.8: Predicted temperature profile for a 90 µm particle with fluid at 1.33 mm/s.

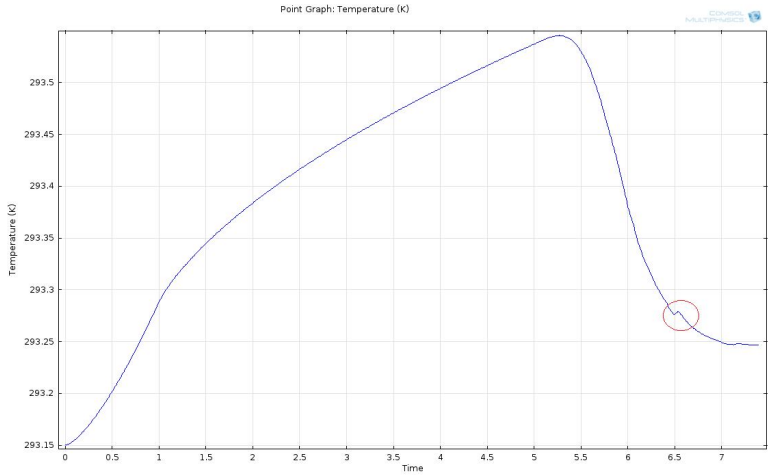

Figure 2.9: Predicted temperature profile for a 90 µm particle with fluid at 2 mm/s.

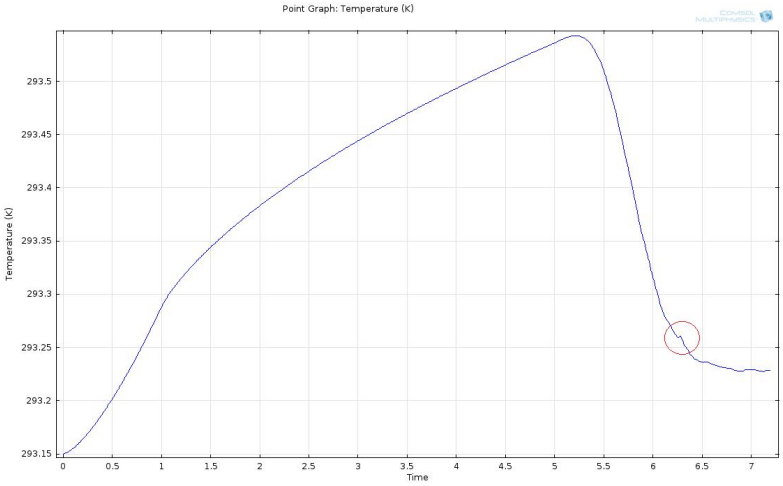

Figure 2.10: Predicted temperature profile for a 90 µm particle with fluid at 2.66 mm/s.

The amplitudes of the peaks in the above plots were determined using the raw data that could be exported from COMSOL in the form of a spreadsheet. Twenty data points on either side of the peak value were summed and averaged to form the mean value or baseline. This mean value was then subtracted from the peak value to determine the amplitude of ΔT. Fig 2.11 shows a magnified plot of the peaks obtained at the three different flow rates. The time on the x-axis does not correspond to the actual time of passage of the bead over the sensor. To plot the magnified signals, the point corresponding to the peak at each flow rate was first located in the raw data. Twenty points on either side of the peak were plotted using MATLAB, which explains the coincidence of the peaks corresponding to the x-axis. It is clear that the peak is widest at the lowest flow rate i.e 6 µl/min, due to higher time of residency of the particle over the heater/sensor. The peaks at 9 µl/min and 12 µl/min are fairly close in trend. A much finer mesh is necessary to provide better resolution of the peak at 12 µl/min, due to the high velocity of the particle. In this case, the mesh size could not be significantly reduced to the difficulty in placing fine quadrilateral elements around the curvature of the particle.

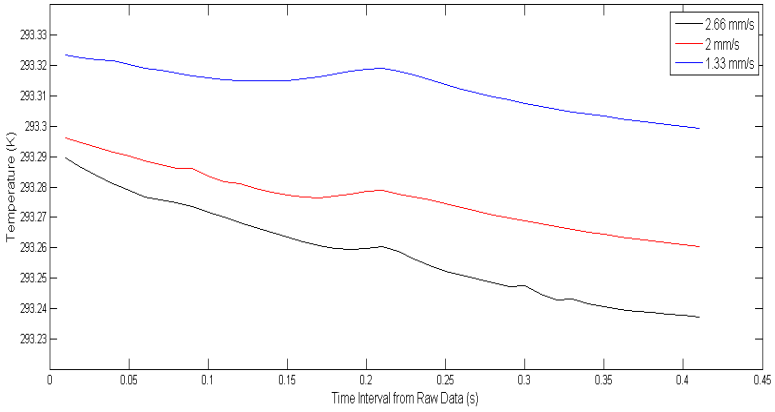

Figure 2.11: Comparison of the predicted signal at 1.33, 2 and 2.66 mm/s.

Table 1 compares computationally and experimentally obtained results. The same table and the analysis following it, are repeated in Chapter 4 so that the experimental and computational sections of this thesis could each be self-contained.

Table 1: Comparison of experimental and computational results obtained in K) at different flow rates and for a simulated heat flux value of 793 W/m^2.

	Computational Results (K)	Experimental Results (K)	
Flow Rate (µl/min)			
12	0.0018	0.0024	0.0005
9	0.0027	0.0046	0.0008
6	0.0064	0.0031	0.0015

Differences were observed in the magnitudes of experimental and computational signals at the same flow rate. The experimental and computational results differed by a factor less than 2 at flow rates of 9 and 12 µl/min. However, the factor was slightly over 2 at 6 µl/min. The amplitude of both the experimental as well as the computational result increased as the flow rate was decreased from 12 µl/min to 9 µl/min. When the flow rate was further decreased to 6 µl/min, the experimental signal dropped while a discrepancy was observed once again in the computational signal which correspondingly increased. The above discrepancy can be attributed to the mesh size and time step chosen in the model as well as the fact that the experimental signals were averaged over multiple peaks while the model contained a single particle and hence had only one peak. Ideally, an optimum mesh size must be determined in the model, for each flow rate, since the deformation of the mesh is different when the particle moves at different velocities. In this case, the mesh sizes were arbitrarily chosen and the minimum mesh size was limited by the software.

At a volumetric flow rate of 6 µl/min (or average velocity of 1.33 mm/s), the maximum mesh size could not be decreased below 11 µm for the above velocity. The time step used was the same for all velocities of the particle and the results may be improved by customizing the time step for each velocity. In addition, the sampling rate was different in the case of the experiments and the model. Data in the experiments was recorded at 50 samples/s or 50 Hz. In case of the model, roughly 100 data points per second were obtained. This resulted in

variations in the averages obtained in the two cases.

In general, the differences in experimental and computational signal can be attributed to the assumptions made in the computational model as well as experimental constraints. The model was 2D in nature and this resulted in an error while extrapolating the physics of particle motion and its response to heat, from the model to the experiment. In the experiments, the particle was 90 μm wide and it occupied less than a third of the channel width. In the simulation, the 2D model is assumed to have a default depth of 1m, which meant that the particle occupied the entire width of the channel as well as the sensor. The particle in the experiment was spherical in shape. The 2D particle in the model is cylindrical when extrapolated to 3D.The particle in the numerical simulation was considered to be perfectly insulated. The polystyrene beads used in the experiment had a low but non-zero value of thermal conductivity. The particle in the model maintained a constant height as it moved through the microchannel. In the experiments, the particles were suspended using glycerol and they were drawn into the channel from a reservoir which did not ensure constant height of the particles.

As the velocity is increased from 9 μl/min to 12 μl/min, the rate of heat transfer from the heater to the fluid increases and this makes the presence of the particle less significant, resulting in a decrease in amplitude.

At a low flow rate of 6 µl/min, the time of residency of the particle over the sensor is maximum, which allows for a temperature gradient to develop in the detection region and the signal at the lowest flow rate is therefore higher than that at the highest flow rate.

In summary, it was found that the experimental and computational results at 9 and 12 µl/min were in reasonable agreement, given the assumptions made while the results at 6 µl/min were close in value but differed in relative trend.

2.4 Numerical accuracy of computational model

For velocities corresponding to flow rates of 6, 9 and 12 µl/min, the maximum mesh element sizes were 11, 12.5 and 13 µm respectively. To control the accuracy of the solver, relative and absolute tolerances were set. The relative tolerance measures the error relative to the size of the variable between iterations. In other words, it limits the fractional change in solution between two iterations. The absolute tolerance is a threshold value of error which becomes significant as the solution approaches zero. It denotes the maximum allowable error when the value of the measured variable is small. The relative and absolute tolerances for the COMSOL solver were set to 1×10^{-3} and 1×10^{-5} respectively.

Chapter 3

Materials and Methods

This chapter discusses the design and construction of the device used for TFC. Over the duration of this research, multiple generations of devices were developed and tested before one was found to be best suited for the application.

3.1 General Device Schematic

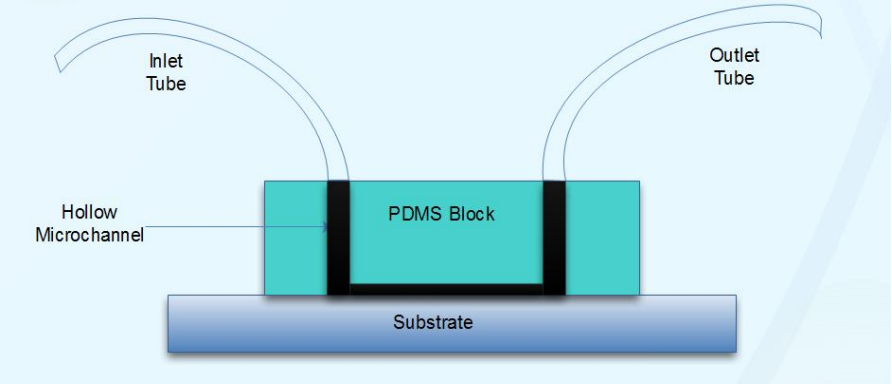

Figure 3.1: Schematic of the device used for TFC. A PDMS block with holes cored out, was bonded to a substrate using oxygen plasma bonding.

Fig 3.1 shows the general layout of the device used for TFC. The basic layout for the device was as follows - a PDMS block with the microchannel fabricated on its lower side through soft lithography, was bonded to the surface of a substrate which had nickel deposited on its upper side. The nickel was deposited to form the RTD in a coil-like pattern. The process of deposition of nickel on the substrate or chip is described in section 3.3. Initial designs used two coils to optimize space on the chip. Only one of these electrodes was used for both heating and sensing, in an experiment. In the early designs of the device, both coils were intended for use simultaneously, with one acting as the heater and the other, the sensor. This complicated design considerations such as the spacing between the heater and the sensor, for accurate detection of a particle. As an improvement on this design, only one of the coils was used as both the heater and the sensor. This approach was tested and deemed adequate for the purpose of the TFC application. If the first coil was damaged during the course of the experiments, the second coil could be used.

3.2 Experimental Setup

Fig. 3.2 describes the experimental setup for TFC. Once the device was fabricated and tubes were inserted into the two ports, one of the tubes was connected to a syringe fixed onto a syringe pump. This formed the inlet tube. The suspension containing the polystyrene beads was pumped through the microchannel through this tube. The other tube was the outlet tube and it was immersed in a container filled with water, to create a stable outlet condition. For the approach using the inlet tube, this outlet condition was critical since the output signal was very sensitive to the exit condition of the fluid. As explained in the sections ahead, the inlet tube was eliminated in the later generations of devices.

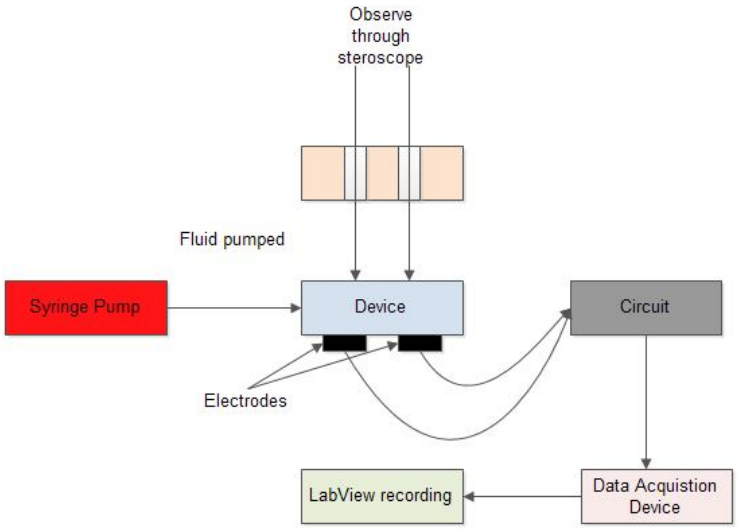

Figure 3.2: Block diagram for the experimental setup of TFC. In the final generation of devices, the circuit and data acquisition device were replaced by a multimeter.

The PDMS block was bonded such that the RTD was one the lower side of the glass substrate. The RTD heated the glass and this heat was then transferred to the fluid by conduction and convection. Fig. 3.3 shows the design of the heater coil used for the first, second and third generation devices. One metallic pin each was attached by means of a fixture to the square pads (not seen in figure) at the ends of the nickel coil. These formed the electrodes across which the output signal was measured. The electrodes were connected to an analog circuit designed on a breadboard. The circuit was designed to take a reference voltage as input and provide a constant current as output. This constant current was fed to the device through the same pair of electrodes mentioned above.

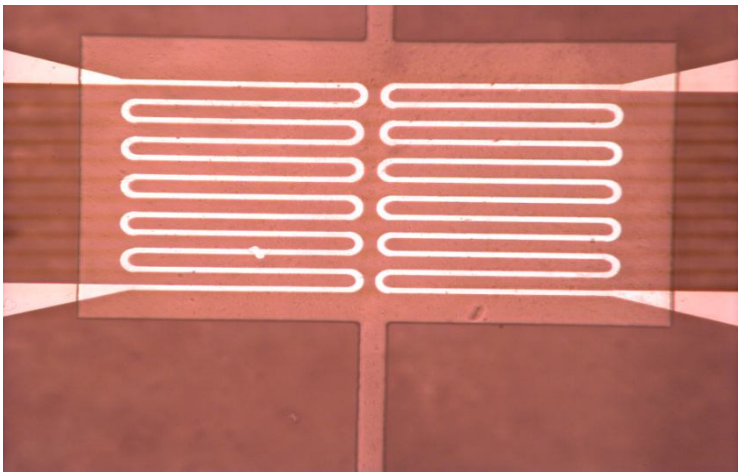

Figure 3.3: Electrodes in the form of coils made by deposition of nickel on a glass substrate. A single coil is used for both heating and sensing. The other coil is provided for reusability of the substrate.

The flow of current through the coil generates heat which is dissipated into the channel. The device was connected to a breadboard circuit and a data acquisition device (DAQ). The signal from the device was recorded using the DAQ which was interfaced with LabView to write the data to an output file. The flow of fluid in the microchannel was observed under a stereoscope. Fig 3.4 shows the fixture that was used to clamp the device and Fig 3.5 shows the device held in the fixture under the stereoscope. The device shown in the figure is a third generation device with the substrate flipped so that the RTD was inside the microchannel.

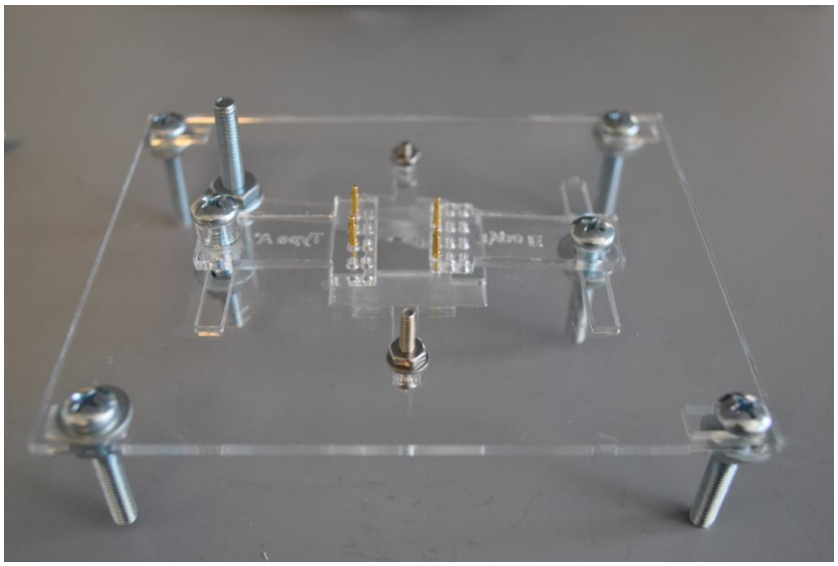

Figure 3.4: The fixture used to hold the device in place during the experiments. The 'golden' pins at the center were the electrodes which made contact with the nickel deposited on the substrate of the device.

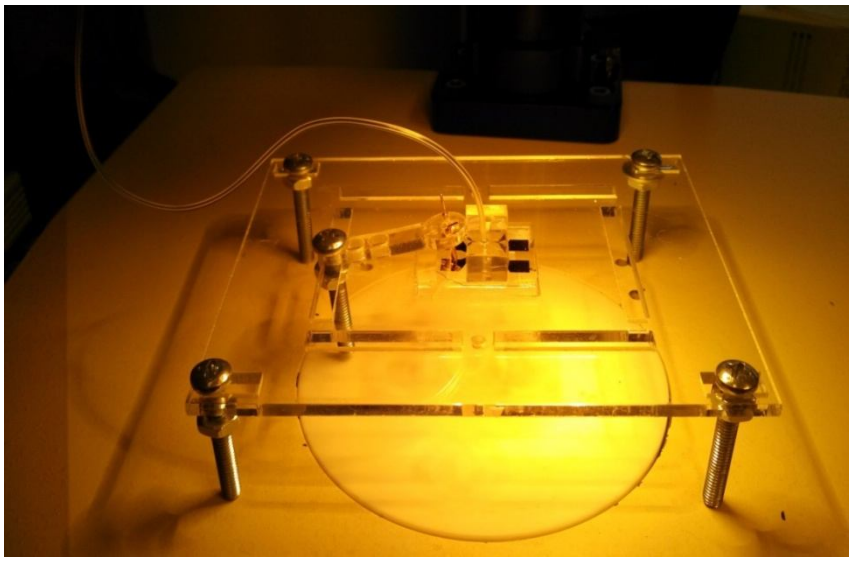

Figure 3.5: Device held in fixture under a stereoscope and connected to a syringe pump (not seen in figure) with electrode pins connected.

3.3 Microfabrication

This section discusses the general procedure to fabricate the device described in the previous section. This consisted of the following steps -

3.3.1 Fabrication of substrate

3.3.2 Fabrication of SU8 master for PDMS channels

3.3.3 PDMS molding

3.3.1 Fabrication of Substrate

For the first, second and third generation devices, a glass substrate was used for the purpose of depositing nickel, which formed the RTD. The substrates were fabricated by Vindhya Kunduru, a Ph.D candidate in Dr. Glenn Walker's lab. The glass substrate was cleaned using acetone and IPA, followed by a baking process for dehydration, which was done at 200°C for 20 minutes. A small amount of photoresist AZ 5214 was added to the substrate, to the size of a quarter dollar coin. The substrate was then subjected to spin coating at 4000 rpm for 45 seconds, which formed a 1.4 µm thick photoresist layer. This was followed by soft baking at 110°C for about a minute. After soft baking, the photoresist layer was exposed under UV light for 8 seconds. To develop the pattern formed, the substrate was immersed in the photoresist developer MIF-CD 26 for 60 seconds and then rinsed with DI water and dried using a nitrogen spray. Fig 3.6 outlines the process flow for the above fabrication.

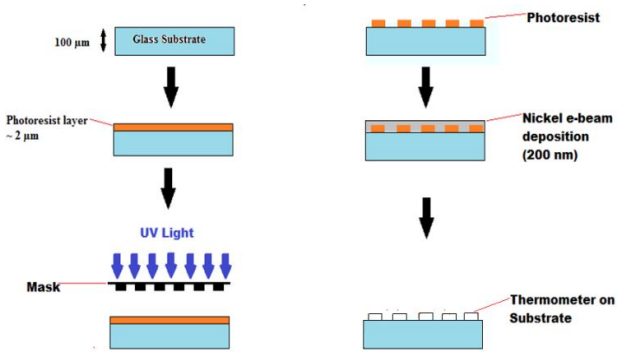

Figure 3.6: Process flow diagram for fabrication of glass substrates. AZ 5214 was used as a negative photoresist. Nickel was deposited to a height of ~ 200 nm using e-beam deposition.

As shown in Fig 3.3, there were two coils on the substrate. To create the second coil, the image was reversed. The substrate was baked at 115°C for 20 minutes. It was then coated with the photoresist and spun at 4000 rpm for 45 seconds, which gave a photoresist layer of about 1.4 µm. The substrate was then soft-baked at 90°C for 2 minutes and later exposed to UV light for 2 seconds. Once the exposure was complete, the substrate was baked again on a hotplate at 116°C for 3 minutes. It was then subjected to flood exposure (without a filter) for 45 seconds. Development of the exposed substrate was done using the developer MIF-CD 26 for 30 seconds with slight agitation. After developing, the substrate was rinsed with DI water and dried with a nitrogen gun.

An electron beam evaporator was used to deposit a 200 nm thick film of nickel (Kurt Lesker, 99.99% pure) on the patterned glass substrates. The nickel-coated substrates were then treated with acetone to lift off nickel from the un-patterned areas, rinsed with DI water, and dried with nitrogen. The sensor was designed to have a nominal resistance of 270 ohms at room temperature.

The final generation of devices were fabricated by bonding PDMS to a silicon substrate on which nickel was deposited to form the sensor. The substrates were supplied by Dr. Chung Hoon Lee at Marquette University. The center of the substrate had a square silicon nitride membrane of 300 µm side.

The nickel pattern was created using e-beam deposition and such that the sensor, in the form of a single meander, was at the center of the membrane (shown later in Fig 3.18).

3.3.2 Fabrication of SU8 master for PDMS Channels

The first step in making PDMS channels was to fabricate a master out of the high-aspect ratio photoresist SU-8. An overview of the process is shown in Fig 3.7. Masks for photolithography were designed using Adobe Illustrator. For the application of TFC, a straight channel with a rectangular cross-section, was deemed to be sufficient. The background of the mask was black in color while the channel was white. When the mask is printed on a transparency, the channel turns out to be transparent while its surroundings are opaque. This is crucial for the process of photolithography when using a negative photoresist.

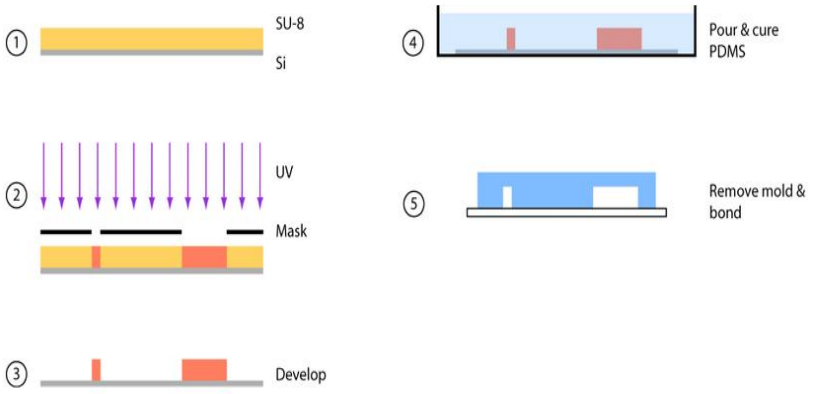

Figure 3.7: Process flow diagram for fabrication of SU8 masters. Source: (Dr. Glenn Walker).

The fabrication of the master, which was then used to fabricate channels in PDMS, was done in a hood located inside a cleanroom facility. The complete fabrication procedure consisted of wafer pre-treatment, photoresist spin-coating, exposure and developing. A 3 inch diameter silicon wafer was first cleaned with acetone and then with IPA**.** This process was repeated 2-3 times. The cleaned substrate was placed on a hotplate that has been heated to 125°C and it was baked for 5 min. The silicon wafer was placed on the vacuum chuck of the spin-coater. The wafer was centered to ensure planar rotations (i.e, until no wobbling was observed). This was done by turning on the vacuum and programming the motor for 500 RPM. With this low RPM, the substrate was made to spin about its center and the tendency to wobble was checked by running a finger along the spinning edge. Once the substrate was centered and the rotations were appropriate, a small amount of SU8-2050 photoresist was poured onto the center region of the substrate until the diameter of a 50 cent coin was approximately achieved. Care was taken to ensure that no air bubbles were present in the liquid mass. The spin-coater was then powered on and the speed was ramped up to 500 rpm at 100 rpm/s. The speed was maintained at 500 rpm for 10 seconds after which the speed was ramped up at 300 rpm/s to 3000 rpm. This speed was maintained for 30 seconds and then the spinner was made to decelerate gradually until it came to rest. Fig 3.8 shows a graph of the thicknesses obtained with different types of photoresist according to the spin speed.

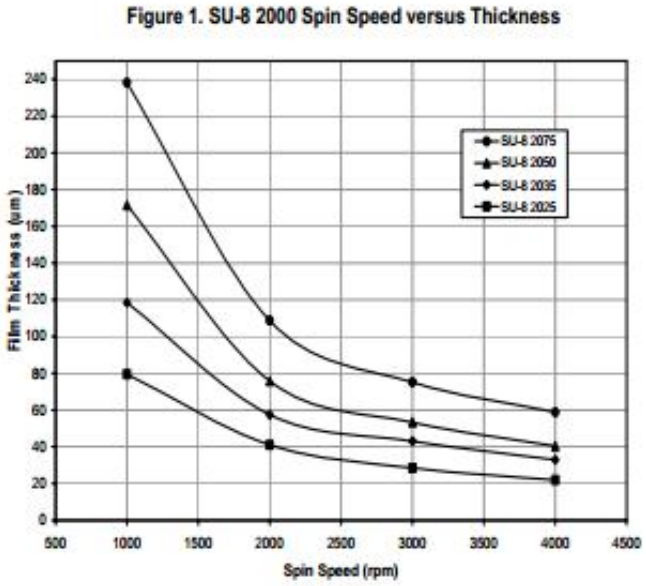

Figure 3.8: Graph of photoresist film thickness obtained vs spin speed. Source: MicroChem

All of the above steps for speed were automated and controlled by means of a program. The process of spinning with the viscous photoresist on the surface of the substrate caused tendrils to form around the edges of the substrate. Any overhanging tendrils were wiped off and the substrate was placed on a hotplate for soft baking. The time and temperature required for soft baking depend on the thickness of the photoresist and are as tabulated in Table 1. The thickness or height of the photoresist determines the height of the microchannel. This is true for the case of a negative photoresist which has the property that any portion of it which is unexposed to light can be removed at the time of developing, leaving the exposed part as the desired shape of the microchannel.

For positive photoresists, the reverse is true, i.e, the exposed part of the photoresist is eliminated at the time of developing while the unexposed part is retained.

Table 2: Soft Baking - time and temperature settings for a range of photoresist thickness. Source: MicroChem.

Thickness (µm)	**Soft Bake Time (mins) 65°C**	**Soft Bake Time (mins) 95°C**
25-40	0-3	5-6
45-80	0-3	6-9
85-110	5	10-20
115-150	5	20-30
160-225	7	30-45

Table 3: Exposure time and intensity settings for a range of photoresist thickness. Source: MicroChem.

Thickness (µm)	**Energy Exposure (mJ/cm^2)**
25-40	150-160
45-80	150-215
85-110	215-240
115-150	240-260
160-225	260-250

Table 4: Post-Exposure Baking Time and temperature settings for a range of photoresist thickness. Source: MicroChem.

Thickness (µm)	PEB Time (mins) 65°C	PEB Time (mins) 95 °C
25-40	1	5-6
45-80	1-2	6-7
85-110	2-5	8-10
115-150	5	10-12
160-225	5	12-15

3.3.3 PDMS Molding

To create the PDMS mold, about 30g of PDMS pre-polymer (PDMS base) was poured into a weigh boat and mixed with 3g of cross-linker. The amount of base used depends on the final thickness of the polymer device desired. A thin layer facilitates bonding with the glass substrate. The mixture was stirred continuously with a plastic fork for about 5 minutes. The weight boat was then placed in a desiccator and subjected to a vacuum until all the air bubbles in the mixture disappeared.

The silicon master was placed in a petri dish made out of aluminum foil and the polymer mixture was poured over it, ensuring that the wafer was completely submerged. Care was taken to ensure that no bubbles were formed at the surface of the mixture in the petri dish.

The petri dish was then placed on a hotplate and the temperature was ramped up to 115°C and maintained for about 5 minutes. Once the PDMS had cured completely, the wafer, combined with the PDMS layer was separated from the petri dish using a spatula and the PDMS layer was peeled off the wafer. Sections of the PDMS with the channel designs on them were cut out and bonded to chips to form devices. Fig 3.9 shows a representative block of PDMS containing straight channels.

Prior to bonding the PDMS mold to the glass chip, both components were cleaned. This was done using Scotch tape. The tape was stuck onto the plain side of chip (the side without the coils) and then carefully peeled off, ensuring that chip does not crack at any point. The procedure was repeated for the PDMS block. Next, both the block and the chip were placed inside an oxygen plasma cleaner with the sides to be bonded, facing upwards. The cleaning equipment was set to high power and run for 20 seconds. The components were removed and aligned under a microscope, while ensuring that the straight fluid channel was aligned with the heater/sensor.

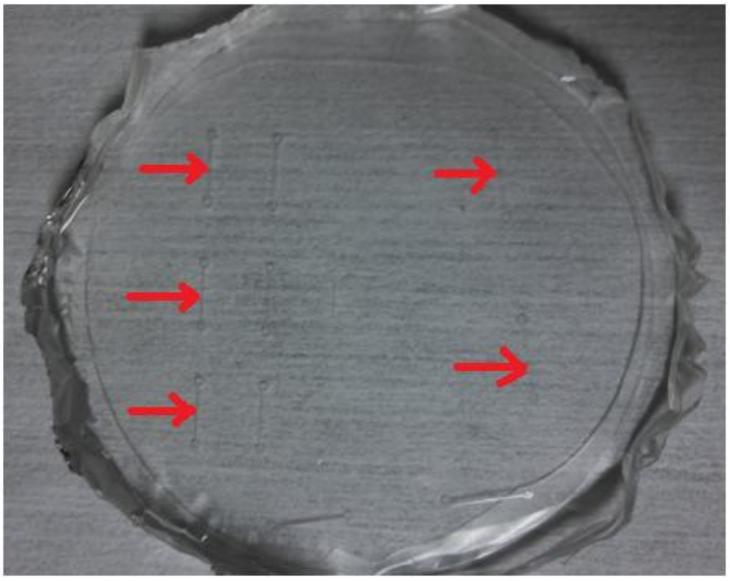

Figure 3.9: Representative channels fabricated in a PDMS mold. Blocks were cut out, each containing one channel, and bonded to a substrate. Red arrows point to the channels formed in the block.

3.4 First Generation Devices

The first generation devices were as described in the device schematic in section 3.1 and with channel design as shown in Fig 3.10. Experiments were run using first 25 µm and later 90 µm polystyrene beads. The 25 µm bead were found to be too small compared to the size of the sensor and the channel. When 90 µm beads were used, it was observed that there were hardly any beads passing through the channel. The solid beads were found to settle in the inlet tube as well as at the bottom of the inlet port. Additionally, the circuit was saturating too quickly for small changes in voltage from the device.

No significant data was obtained for solid beads through the use of these devices. However, encouraging data was collected through the use of the T-junction channel shown in Fig 3.11. This T-junction device was used to produce water-slugs by passing DI water through one inlet and air through the other. The results are shown in Chapter 4. The circuit used for these devices is described in section 3.4.1.

(a)

(b)

Figure 3.10: Early designs for the mask used in channel fabrication. (a) The angled channels were incorporated to allow hydrodynamic focusing of the solid particles. (b) The angled channels were replaced by a loop to reduce the number of syringes required.

Figure 3.11: Mask with T-junction channel included for testing the device using water-slugs. The channels in the first and second row are 1 mm wide. The channels in the third row are 0.3 mm wide. The remaining channels were not used.

In the first generation devices, the width of the heater was 1 mm and for most of the above designs, it was too large compared to the width of the channels. The 40 μm channels occupied less than a tenth of the heater space. The 1 mm channels (Fig 3.11) matched the width of heater and so this design was retained for the next generation of devices. However, the channel for hydrodynamic focusing was found to be redundant since the concentration of the suspension and size of beads can be controlled to obtain the desired behaviour of beads. Fig 3.12 shows the completely assembled first generation device.

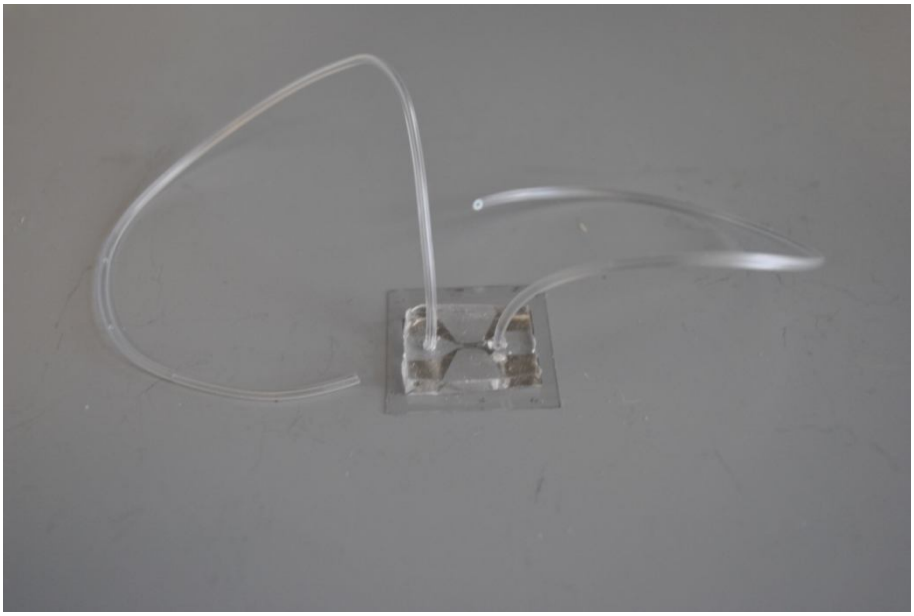

Figure 3.12: The completed first generation device. PDMS block thickness and tube length were optimized in later designs.

3.4.1 Circuit for First Generation Devices

The analog breadboard circuit consisted of two modules- the heating circuit and the sensing circuit. The heating circuit was used to supply a constant current of 8 mA to the device through the electrodes connected to the pads. The passage of current through the nickel coil produces Joule heating according to eq. (25). The heat produced from the coils heats the fluid-particle suspension flowing through the channel.

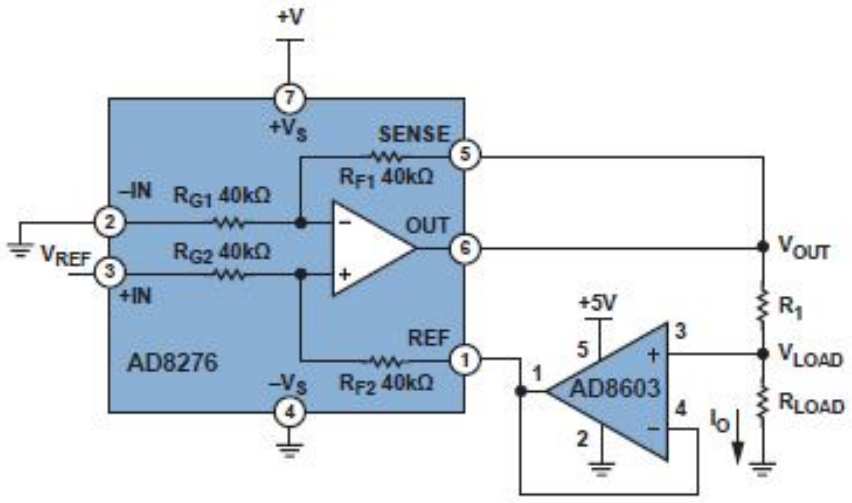

Figure 3.13: Constant current circuit used to power the fabricated device. Source: (Zhao et.al 2009).

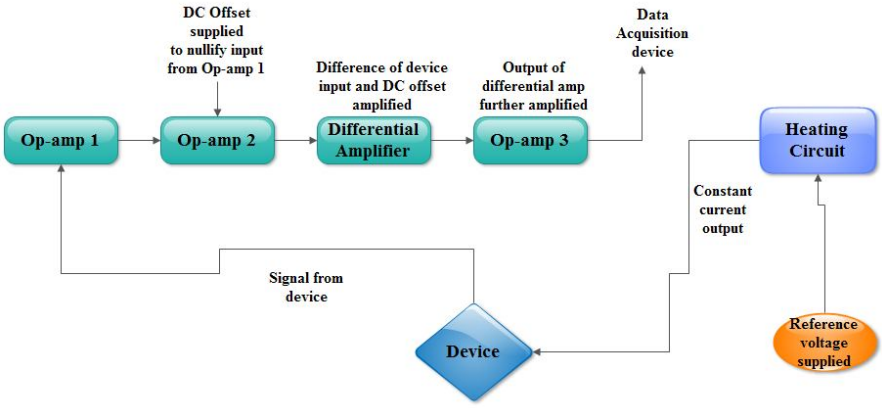

Figure 3.14: Block diagram of the first generation of the analog circuit that was constructed on a breadboard and connected to a data acquisition system (NI USB-6009).

The device resistance forms R_{LOAD} shown in Fig 3.14. The circuit was operated with inputs of +15 V and -15V supplied from an Agilent E3649A power source. The heating electrodes of the device were connected across the heating or excitation circuit and a reference voltage of 0.6 V was provided to the circuit. This produced a constant current of about 6 mA through the coils. As per the working theory described in section 3.2, differential heating of fluid and solids was anticipated, which would produce a change in temperature in the region above the heater in the channel and this would be sensed by the electrodes. The fluctuation was expected to be too small to notice without aid and hence the signal was amplified via the sensing circuit before it was recorded. The sensing circuit consisted of three instrumentation amplifiers and a differential amplifier. The output signal was fed to the first instrumentation amplifier and offset by a DC voltage supplied to a second amplifier. This DC voltage was equal in sign and magnitude to the signal. The function of the differential amplifier was to multiply the difference of the signal and the offset by its gain. The result from this amplifier was fed to the third instrumentation amplifier which further multiplied the result by its gain. The output of the third instrumentation amplifier was fed to both the oscilloscope as well as a data acquisition device (DAQ- NI USB-6009).The device was interfaced with the software LabView to monitor and record signals from the device.

With the first generation constant circuit, it was found that the sensitivity to changes in temperature around the electrodes was good. The test was performed by blowing air over the electrodes. The cold air was observed to produce a drop in temperature of the electrodes.

This could be gauged by a sharp drop in voltage on an Oscilloscope connected to the circuit.

3.5 Second Generation Devices

To overcome the problem of tube clogging in the first generation of devices, an alternative was proposed and successfully tested. In these second generation devices, the inlet tube was eliminated and the inlet port was widened. Once it was bonded, the widened port served as a reservoir or well for the suspension containing beads, as shown in Fig 3.9. The syringe pump was then connected to the outlet tube and instead of pumping, the suspension was withdrawn through the channel. This was found to greatly enhance the number of beads passing through the channel. However, the beads still tended to settle quickly in the reservoir. To counter this problem, the beads were balanced using glycerol, as described in section 3.8. By balancing the densities of the beads and the fluid, the beads could be suspended indefinitely. Narrower channels of 0.3 mm width were used in the second generation of devices.

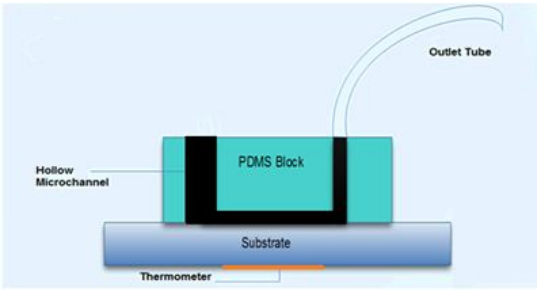

Figure 3.15: Second generation of devices with the inlet tube eliminated and replaced with a large cored out vertical column that serves as a reservoir for the suspension.

Despite observing several beads passing through the channel during a specific time interval, no signal was obtained with these devices. The substrate was determined as the cause for the lack of data. The glass substrate was too thick to register a change in temperature due to the passage of a 90 µm bead above it. This relatively large thickness was likely to make any signal from the device or in other words, the sensitivity of the device was low. These problems were eliminated in the third generation of devices. The circuit used for the second generation of devices is described in the following section.

3.5.1 Circuit for Second Generation Devices

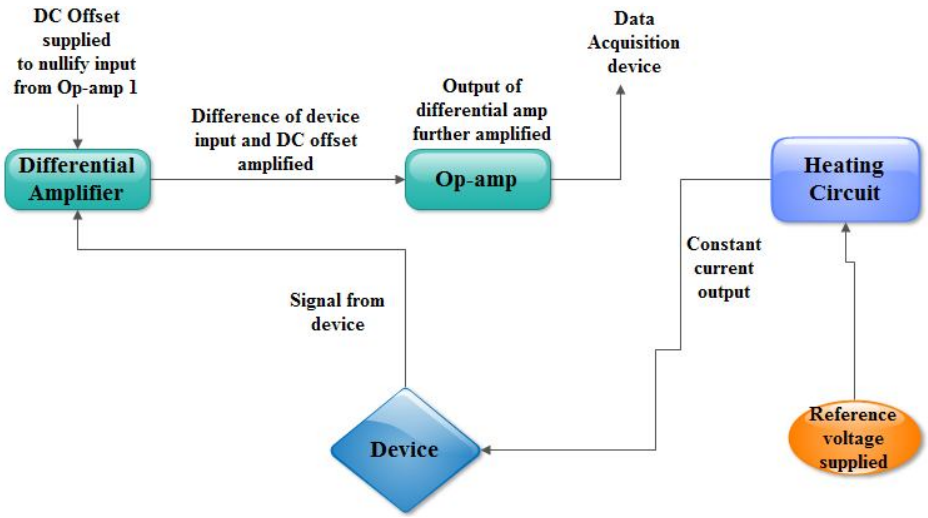

Figure 3.16: Block diagram of the second generation of constant current circuits used. The additional instrumentation amplifiers from the first generation circuit were eliminated to prevent saturation of the circuit.

To overcome the problem of saturation in the first generation circuit, the instrumentation amplifiers were eliminated in the second generation circuits. The signal from the device and the DC offset were both fed to the first differential amplifier which multiplied their difference by its gain and fed the result to an instrumentation amplifier. The amplified output from the op-amp was fed to the oscilloscope and the DAQ.

3.6 Third Generation Devices

In these devices, the PDMS block from the second generation was retained. The substrate was flipped over so that the PDMS block was now bonded on the side that contained the nickel RTD. The 0.3 mm channels shown in Fig 3.9. were used for this generation of devices. The coil of the RTD was inside the microchannel and this was expected to increase the sensitivity of the device significantly. However, despite numerous experimental runs, no repeatable data was obtained. A diagnosis revealed two problems- the RTD was still in contact with a large thermal mass (glass) on one side and the circuit noise remained the same with the substrate flipped.

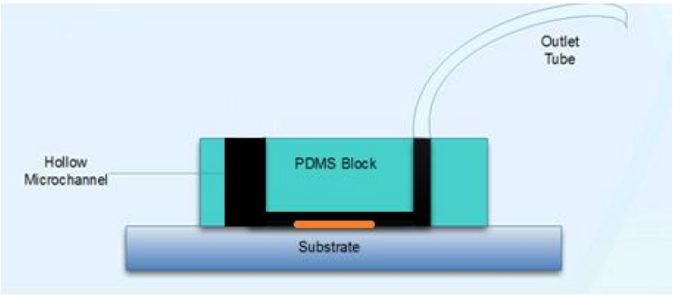

Figure 3.17: Third generation of devices which differed from the second generation only in the orientation of the substrate. The substrate was flipped over so that the RTD was inside the channel.

3.6.1 Circuit for Third Generation Devices

The circuit used for the third generation of devices was the same as that used for the previous generation.

3.7 Fourth Generation Devices

The fourth generation devices formed the final generation of devices fabricated. The substrate used for these devices is as shown in Fig 3.18. The channel design from the third generation devices was retained. The breadboard circuit used was eliminated and the signal from the device was recorded directly by using a multimeter (Agilent 34410A) interfaced with LabView. The multimeter was setup to use the 2-wire resistance method to measure the resistance change of the RTD corresponding to a change in its temperature. The recorded data was plotted using MATLAB. Repeatable results were obtained using these devices, for 90 µm beads, at three different flow rates of 6, 9 and 12 µl/min.

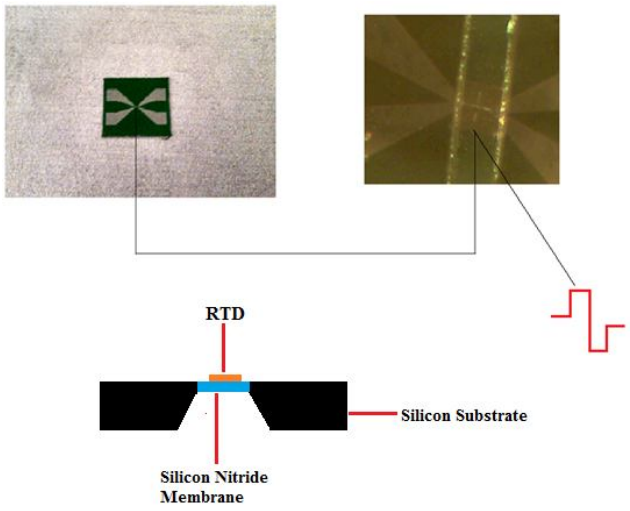

Figure 3.18: (top left) Silicon substrate patterned with nickel and (top right) magnified image of the sensor on the substrate. (bottom right) Diagram of enlarged sensor pattern. The width of the nickel strip was approximately 10 µm. (bottom left) 2D schematic of substrate.

3.8 Preparation of Sample Suspension and Flow Conditions

The sample used for the experiments was a dilute suspension of polystyrene beads (Polysciences- Polybead Microspheres - 90µm) in DI water. A bead-to-water concentration of 1:500 was used. The diluteness of the suspension ensured that the beads were sparse enough to allow only one bead in the detection region at a given instant. To avoid settling of beads before they entered the channel, a density balancing medium was used to ensure that the beads remain suspended indefinitely in the carrier fluid.

The balancing agent used was glycerol and quantities of the different substances were added according to the formula -

$$D = \frac{V_1 d_1 + V_2 d_2}{V_1 + V_2} \tag{26}$$

where D is the density of the final suspension, which must equal the density of the beads for them to be suspended. V_1 ,d_1, V_2 and d_2 are the volumes and densities of the carrier fluid and balancing agent respectively. For any arbitrarily chosen volume of the carrier fluid, the above formula gives the volume of the balancing medium required, when the density of the solid particles is known.

For the first generation devices, separate suspensions were prepared using bead sizes of 25 µm and 90 µm. The 25 µm particles were too small to elicit any response from the sensor. Hence, with the size of the heater coils in mind, the 90 µm bead suspension was chosen for subsequent experiments.

Care was taken to ensure that the suspension was well balanced using glycerol so that the beads remained suspended indefinitely. Through a process of trial and error, it was found that flow rates of 6 µl/min and above were high enough to draw beads out from the well in sufficient numbers. The flow rates for experiments with the second, third and final generation devices were then fixed at 6, 9 and 12 µl/min.

Chapter 4

Results and Discussion

Repeatable experimental results were obtained with the final generation devices. Results were obtained for three arbitrarily chosen flow rates of 6, 9 and 12 µl/min. Data was recorded for 30 seconds in case of solid particles. Test results with the first generation of results are also presented in the following section.

4.1 Results with First, Second and Third Generation Devices

The results from a 'breath test' and effect of change of flow rate on output signal were similar for the first three generations of devices. In the 'breath test', air was blown in short bursts over the electrodes and the corresponding fluctuation in the signal was observed and recorded. The sharp peaks (Fig 4.1) confirmed that the circuit responded to a significant change in temperature of the electrodes. However, such a temperature change was not observed with the solid beads.

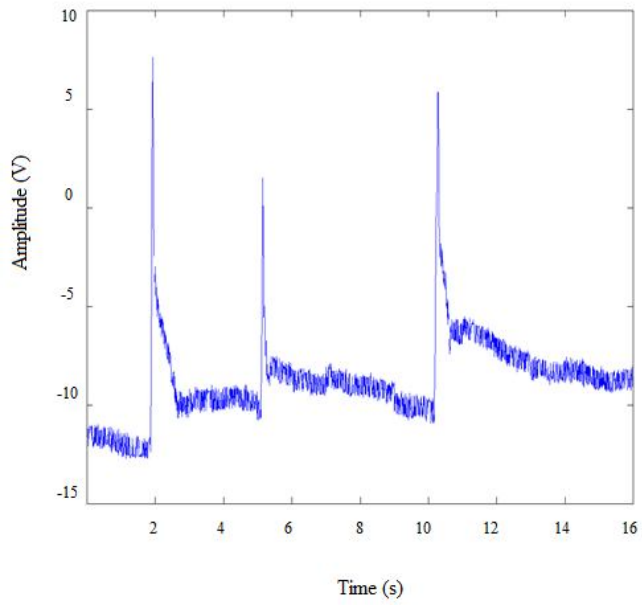

Figure 4.1: MATLAB plot of voltage amplitude against time. The sharp peaks indicate the response to a disturbance introduced into the circuit by blowing air over it.

The next step was to test the device and the response of the circuit to different flow rates. From the theory of convection, it is known that convection heat transfer off a heated substrate depends on the velocity of the fluid and so the signal was expected to change with varying flow rates. DI water with no particles suspended was made to flow through the channel at flow rates of 1, 5, 7 and 10 µl/min. Fig 4.2. shows the variation in signal with the flow rates.

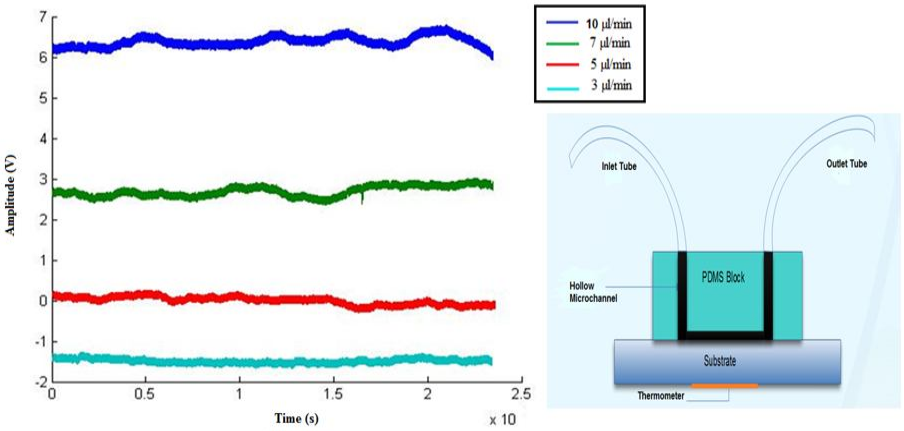

Figure 4.2: (left) Shift in baseline voltage (y-axis) due to change in flow rates. (right) Schematic of device used for the measurement. Fluid was pumped in through the inlet tube at different flow rates and the corresponding signal was recorded.

4.2 Results with Water-Slugs

Before passing solid beads into the channel, the sensor was tested using a T-junction channel which would produce water-slugs. Water-slugs are easier to pass in a repeatable manner into the channel and they are easier to detect because they are large compared to the sensor. The air flow rate was 122 µl/min and that of DI water was 10 µl/min. Results with water-slugs are as shown in Fig 4.3. Distinct signals were obtained due to the size of the slugs and the time interval between generation of slugs.

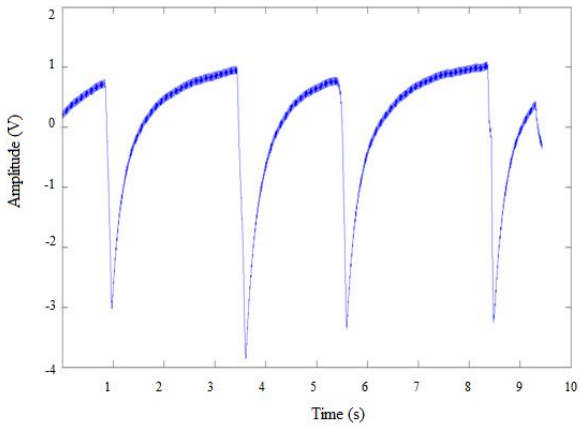

Figure 4.3: Detection of DI water-slugs in the microchannel. The size of the slugs relative to the channel and the sensor, ensured distinct signals.

4.3 Results with Fourth Generation Devices

With the final generation of device that had silicon substrates, results were obtained with 90 µm beads at three different flow rates. The output signal contained a low-noise signal with peaks produced at the instants at which a solid bead passed over the sensor. Fig 4.4 (a), (b) and (c) show the results obtained with 90 µm particles at flow rates of 12, 9 and 6 µl/min respectively. At 12 µl/min, more peaks were observed since the high flow rate allowed more beads to be drawn into the channel.

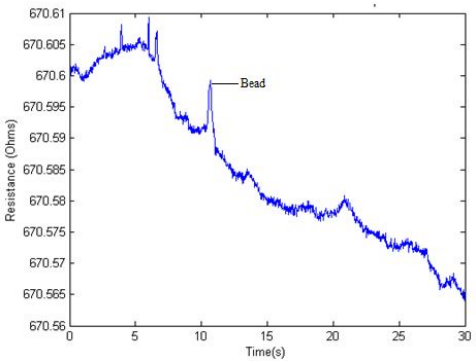

(a)

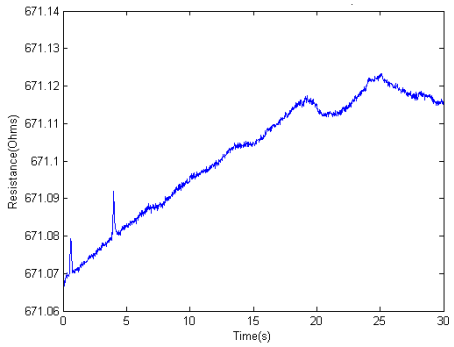

(b)

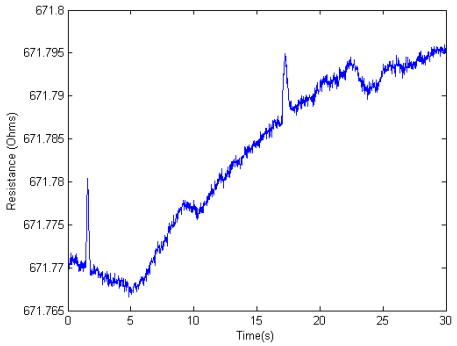

(c)

Figure 4.4: 90 µm beads detected at (a) 12 µl/min (b) 9 µl/min and (c) 6 µl/min.

4.4 Discussion

With the first generation of devices no significant data was obtained with solid particles due to the clogging of the particles in the inlet tube and at the bottom of the inlet port. In addition, the analog circuit designed was found to saturate often, thus preventing any data collection.

For the second generation of devices, the width of the channel was reduced and smaller sensors were used. Other problems with the first generation of devices, such as difficulty in passage of beads, was reduced by creating a reservoir in the PDMS block and withdrawing the beads through the channel instead of pumping them through it. However, these devices did not produce any noteworthy results. This was because the presence of the glass substrate between the RTD and the channel reduced the heat dissipated into the channel.

For the third generation devices, an attempt was made to facilitate detection of the particles by bonding the PDMS block to the substrate on the side of the nickel RTD. The presence of the heater inside the channel was expected to produce higher temperatures and make it easier to recorded temperature changes with the analog circuit. However, this change in orientation of the substrate proved to be insufficient to enumerate particles with this generation of devices. Despite eliminating the problem with saturation of the circuit, it was still not sensitive enough to register the presence of a solid particle in the small time interval that the particle passed over the RTD.

In the final generation of devices, a multimeter was used to measure resistance changes in the RTD due to a changes in its temperature. The multimeter was considerably more sensitive than the analog circuit constructed and along with the approach in the third generation of devices, was instrumental in achieving the expected results. The multimeter had precision up to 6 decimal places, which made it suitable for the detection of 90 μm particles, which produced signals on the order of 0.001 K.

The size of the bead relative to that of the sensor was an important parameter in the use of this device. In the case of 90μm beads, the distance between the sensor (located in the center of the channel) and the channel wall, was larger than the diameter of the beads. It was found that beads passing the sensor along the edge of the channel were sometimes undetected or the signal was vague. As seen in Fig 4.4, the experimental results with solid particles were obtained in the form of change in resistance. This change was converted to a temperature difference using the relation

$$R_f = R_0\left(1+\alpha\,\Delta T\right) \tag{27}$$

or

$$\Delta R / R_0 = \alpha\,\Delta T \tag{28}$$

where R_f = final resistance, R_0= initial resistance, $\Delta R = R_f - R_0$, ΔT = difference in temperature and α = temperature coefficient of resistance for RTD = 3 x 10^{-3} K^{-1}.

The raw data was analyzed and the points corresponding to the peak values were located. Twenty data points on either side of the peak value were summed up and averaged to calculate R_0, which formed the mean value or baseline. R_f was the peak value. Using these values, ΔT was calculated for each peak. The arithmetic mean and standard deviation of the different values of ΔT were calculated to determine the average amplitude of temperature change at each flow rate. Raw data for computational results were analyzed in a similar manner to determine the average amplitude of the signal. The averaged experimental and computational results are as tabulated in Table 5. Standard deviations for the averaged experimental peak amplitudes were found to be 15×10^{-4} at 6 µl/min, 8.79×10^{-4} at 9 µl/min and 5×10^{-4} at 12 µl/min. The numbers of particles detected at 6 µl/min and 9 µl/min were small, leading to larger standard deviations.

The full width at half maximum (FWHM) of the peaks at each of the flow rates were also calculated. Fig 4.5 shows a representative plot of the FWHM for a given peak. Intuitively, it can be inferred that lower time of residency of the particle with increase in flow rate means that the peaks should become narrower as the flow rate increases. To calculate the FWHM, 40 points, 20 on either side of the peak value were fit to a normal distribution using the 'fitdist' function in MATLAB.

The output of the function is the mean and standard deviation of the data with respect to the vertical axis of symmetry. The FWHM was then calculated using the relation

$$FWHM = 2.35482 * \sigma \quad (29)$$

where σ is the standard deviation.

The FWHM at 6, 9 and 12 µl/min were 3.11×10^{-3}, 2.98×10^{-3} and 1.96×10^{-3} respectively. The standard deviations for the different peaks at each flow rate were arithmetically averaged to find the FWHM. The averaged FWHMs were found to decrease with increase in flow rate, indicating a reduction in time of residency of the particle over the heater/sensor.

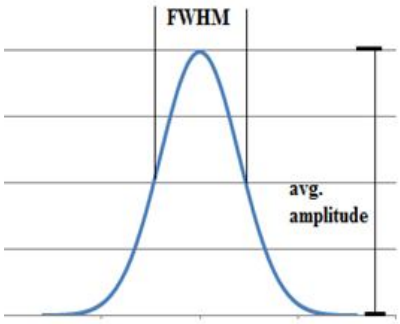

Figure 4.5: Representative illustration of full width at half maximum (FWHM) for a signal peak.

Table 5: Comparison of experimental and computational results at a simulated heat flux value of 793 W/m^2.

	Computational Results (K)	Experimental Results (K)
Flow Rate (µl/min)		
12	0.0018	0.0024 ∓ 0.0005
9	0.0027	0.0046 ∓ 0.0008
6	0.0064	0.0031 ∓ 0.0015

Table 5 compares the temperature difference (ΔT) obtained from the experiments with the same parameter from the numerical simulation. The numerical differences in experimental and computational results can be largely attributed to the assumptions made in the computational model as well as some factors in the experiments such as lateral distance between the particle and the sensor, and different vertical distances of the particle from the sensor during the experiment and numerical simulation. The particle in the model is considered perfectly insulating but the particles in the experiment have a low but non-zero thermal conductivity. An error can be expected while extrapolating the results of a 2D model to the spherical particles used in the experiments. This is because the particle in the experiment occupied roughly a third of the channel width while an extrapolation of a 2D model to 3D would mean that the particle extends across the width of the channel and is cylindrical in shape.

In addition, the sampling rate in the experiments was 50 Hz whereas in the numerical simulation, ~ 100 data points were obtained per second. This led to variations in statistical analysis of results in the two cases.

As the velocity of the fluid and the particle increases from 9 µl/min to 12 µl/min, the amplitude of the signal is expected to decrease because the fluid now carries away heat at a higher rate and this compensates for the presence of the particle. At a lower velocity of 6 µl/min, the time of residency of the particle over the sensor is higher but the fluid absorbs lesser heat from the heater and so the difference between the temperatures of the fluid and the particle is expected to be less than that at 9 µl/min. However, while this phenomenon was observed in the experiments, it was not seen in the numerical simulation at 6 µl/min. As explained in Chapter 2, the constraint on the maximum mesh element size was found to be an important factor in this discrepancy. An optimized mesh size and time step is preferred for each flow rate due to the difference in deformation of the mesh elements according to the speed of the particle. From the experimental and computational results, it can be seen that the principle of TFC and the performance of the device can be verified at 9 µl/min and 12 µl/min. However, further investigation is necessary to understand the process at 6 µl/min.

Chapter 5

Conclusions

The technique of Thermal Flow Cytometry was successfully introduced and proven for detection of solid particles in a microchannel. Solid polystyrene beads were enumerated with reasonable accuracy from a sample suspension. The technique was also found to be applicable for counting slugs of DI water within a microchannel.

5.1 Limitations of TFC

Although TFC has advantages over several other particle counting techniques, it has some drawbacks as well. The accuracy drops considerably when the sample suspension has a high concentration of solids. If this concentration is reasonably high, the signal is distorted and the procedure is then invalid. The output signal is extremely sensitive to the presence of unwanted or 'foreign' medium in the channel, such as air bubbles and debris. The solid bead must occupy a significant fraction of the sensor for it to be detected, typically 0.5 or more. If the technique of withdrawing the mixture into the channel is used, the flow rate must be sufficiently high for enough beads to be drawn into the channel. If the channel is not primed before each run, then the beads clogged up in the reservoir from the previous runs obstruct the passage of new beads and reduce the accuracy of the procedure.

5.2 Future Directions

While the goal of this research was to provide proof-of-concept for using thermal effects to quantify solid particles in a mixture, a more detailed investigation is required to fully understand the parameters that govern this process. For instance, an exact ratio of particle size to sensor size is imperative for the accurate design of sensors for this process. The effect of much higher and much lower flow rates than those used here will provide better insight into the limits of this procedure. A more effective technique to draw beads into the channel without clogging the reservoir will also greatly improve the accuracy of the technique. The sensor used for this research was a coil with a single meander. If the number of turns of the coil are increased, it could possibly allow better resolution of signals from particles of different sizes. A more detailed analysis of the process is required at a flow rate of 6 µl/min to validate the computational results at this flow rate.

References

Altendorf, E., Iverson, E., Schutte, D., Weigl, B., Osborn, T., Sabeti, R. & Yager, P. 1996, *Optical flow cytometry utilizing microfabricated silicon flow channels,* SPIE - Int Soc Optical Engineering, Bellingham; PO Box 10, Bellingham, WA 98227-0010.

Bonetta, L. 2005, "Flow cytometry smaller and better", *Nature Methods,* vol. 2, pp. 785-795

Carbonaro, A. & Sohn, L.L. 2005, "*A resistive-pulse sensor chip for multianalyte immunoassays",* The Royal Society of Chemistry, vol.5, pp.1155-1160

Chapman, G.V. 2000, "Instrumentation for flow cytometry", *Journal of immunological methods,* vol. 243, no. 1–2, pp. 3-12.

Cui, L., Zhang, T. & Morgan, H. 2002, "Optical particle detection integrated in a dielectrophoretic lab-on-a-chip", *Journal of Micromechanics and Microengineering,* vol. 12, no. 1, pp. 7-12.

Coulter, W.H 1953, "Means for Counting Particles Suspended in a Fluid", US Patent 2,656,508

Gaur, U. & Wunderlich, B. 1982, "Heat-Capacity and Other Thermodynamic Properties of Linear Macromolecules .5. Polystyrene", *Journal of Physical and Chemical Reference Data,* vol. 11, no. 2, pp. 313-325.

Gawad, S., Schild, L. & Renaud, P. 2001, "Micromachined impedance spectroscopy flow cytometer for cell analysis and particle sizing", *Lab on a Chip,* vol. 1, no. 1, pp. 76-82.

Givan, A.L. 2001, *Flow Cytometry : First Principles,* Wiley-Liss.

Graves, S.W., Habbersett, R.C. & Nolan, J.P. 2001, "A dynamic inline sample thermoregulation unit for flow cytometry", *Cytometry,* vol. 43, no. 1, pp. 23-30.

Jagtiani, A., Zhe, J., Hu, J. & Carletta, J. 2006, "Detection and counting of micro-scale particles and pollen using a multi-aperture Coulter counter", *Measurement Science & Technology,* vol. 17, no. 7, pp. 1706-1714.

Koch, M., Evans, A.G.R. & Brunnschweiler, A. 1999, "Design and fabrication of a micromachined Coulter counter", *Journal of Micromechanics and Microengineering*, vol. 9, pp. 159.

Kummrow, A., Theisen, J., Frankowski, M., Tuchscheerer, A., Yildirim, H., Brattke, K., Schmidt, M. & Neukammer, J. 2009, "Microfluidic structures for flow cytometric analysis of hydrodynamically focussed blood cells fabricated by ultraprecision micromachining", *Lab on a Chip*, vol. 9, no. 7, pp. 972-981.

Larsen, U.D., Blankenstein, G. & Branebjerg, J. 1997, "Microchip Coulter particle counter", *Solid State Sensors and Actuators, 1997. TRANSDUCERS '97 Chicago., 1997 International Conference on*, pp. 1319.

Lee, W., Fon, W., Axelrod, B.W. & Roukes, M.L. 2009, "High-sensitivity microfluidic calorimeters for biological and chemical applications", *Proceedings of the National Academy of Sciences*, vol. 106, no. 36, pp. 15225-15230.

Lin, C. & Lee, G. 2003, "Micromachined flow cytometers with embedded etched optic fibers for optical detection", *Journal of Micromechanics and Microengineering*, vol. 13, no. 3, pp. 447-453.

Marcus, S. & Blaine, R. 1994, "Thermal-Conductivity of Polymers, Glasses and Ceramics by Modulated Dsc", *Thermochimica Acta*, vol. 243, no. 2, pp. 231-239.

McPherson, A. & Walker, G. 2010, "A microfluidic passive pumping Coulter counter", *Microfluidics and Nanofluidics*, vol. 9, no. 4, pp. 897-904.

Moldavan, A. 1934, "Photo-Electric Technique for the Counting of Microscopical Cells", *Science*, vol. 80, no. 2069, pp. 188-189.

Murali, S., Jagtiani, A.V., Xia, X., Carletta, J. & Zhe, J. 2009, "A microfluidic Coulter counting device for metal wear detection in lubrication oil", *Review of Scientific Instruments*, vol. 80, no. 1, pp. 016105.

Pamme, N., Koyama, R., Manz, A. 2003, "Counting and sizing of particles and particle agglomerates in a microfluidic device using laser light scattering: application to a particle-enhanced immunoassay", *Lab on a Chip*, vol. 3, no. 3, pp.187-192.

Patel, A.R., Lau, D. & Liu, J. 2012, "Quantification and Characterization of Micrometer and Submicrometer Subvisible Particles in Protein Therapeutics by Use of a Suspended Microchannel Resonator", *Analytical Chemistry*, vol. 84, no. 15, pp. 6833-6840.

Rodriguez-Trujillo, R., Mills, C.A., Samitier, J. & Gomila, G. 2007, "Low cost micro-Coulter counter with hydrodynamic focusing", *Microfluidics and Nanofluidics,* vol. 3, no. 2, pp. 171-176.

Shapiro, H.M., 2003, "Practical flow cytometry", *Wiley-Liss*, 4th Edition, pp 73-100

Xiang, Q., Xuan, X., Xu, B., Li, D. 2005, "Multi-Functional Particle Detection with Embedded Optical Fibers in a Poly(dimethylsiloxane) Chip", *Instrumentation Science & Technology,* vol. 33, no.5, pp.597-607.

Xu, D., Kang, Y., Sridhar, M., Hmelo, A.B., Feldman, L.C., Li, D. & Li, D. 2007, "Wide-spectrum, ultrasensitive fluidic sensors with amplification from both fluidic circuits and metal oxide semiconductor field effect transistors", *Applied Physics Letters,* vol. 91, no. 1, pp. 013901.

Zhang, H., Chon, C., Pan, X. & Li, D. 2009, "Methods for counting particles in microfluidic applications", *Microfluidics and Nanofluidics,* vol. 7, no. 6, pp. 739-749.

Zhao, N., Malik, R., Liao, W. 2009, "Difference Amplifier Forms Heart of Precision Current Source", *Analog Dialogue*vol. 43 no. 3, pp. 22-24.

Zheng, S., Liu, M. & Tai, Y. 2008, "Micro coulter counters with platinum black electroplated electrodes for human blood cell sensing", *Biomedical Microdevices,* vol. 10, no. 2, pp. 221-231.